

# Unified Polymerization Mechanism for the Assembly of ASC-Dependent Inflammasomes

Alvin Lu,<sup>1,2,8</sup> Venkat Giri Magupalli,<sup>1,2,8</sup> Jianbin Ruan,<sup>1,2,8</sup> Qian Yin,<sup>1,2</sup> Maninjay K. Atianand,<sup>3</sup> Matthijn R. Vos,<sup>4</sup> Gunnar F. Schröder,<sup>5,6</sup> Katherine A. Fitzgerald,<sup>3</sup> Hao Wu,<sup>1,2,\*</sup> and Edward H. Egelman<sup>7</sup>

<sup>1</sup>Department of Biological Chemistry and Molecular Pharmacology, Harvard Medical School, Boston, MA 02115, USA

<sup>2</sup>Program in Cellular and Molecular Medicine, Boston Children's Hospital, Boston, MA 02115, USA

<sup>3</sup>Division of Infectious Diseases and Immunology, Department of Medicine, University of Massachusetts Medical School, Worcester, MA 01655, USA

<sup>4</sup>FEI Company, Nanoport Europe, 5651 GG Eindhoven, the Netherlands

<sup>5</sup>Institute of Complex Systems, Forschungszentrum Jülich, 52425 Jülich, Germany

<sup>6</sup>Physics Department, Heinrich-Heine Universität Düsseldorf, 40225 Düsseldorf, Germany

<sup>7</sup>Department of Biochemistry and Molecular Genetics, University of Virginia, Charlottesville, VA 22908, USA

<sup>8</sup>Co-first authors

\*Correspondence: [hao.wu@childrens.harvard.edu](mailto:hao.wu@childrens.harvard.edu)

<http://dx.doi.org/10.1016/j.cell.2014.02.008>

## SUMMARY

Inflammasomes elicit host defense inside cells by activating caspase-1 for cytokine maturation and cell death. AIM2 and NLRP3 are representative sensor proteins in two major families of inflammasomes. The adaptor protein ASC bridges the sensor proteins and caspase-1 to form ternary inflammasome complexes, achieved through pyrin domain (PYD) interactions between sensors and ASC and through caspase activation and recruitment domain (CARD) interactions between ASC and caspase-1. We found that PYD and CARD both form filaments. Activated AIM2 and NLRP3 nucleate PYD filaments of ASC, which, in turn, cluster the CARD of ASC. ASC thus nucleates CARD filaments of caspase-1, leading to proximity-induced activation. Endogenous NLRP3 inflammasome is also filamentous. The cryoelectron microscopy structure of ASC<sup>PYD</sup> filament at near-atomic resolution provides a template for homo- and hetero-PYD/PYD associations, as confirmed by structure-guided mutagenesis. We propose that ASC-dependent inflammasomes in both families share a unified assembly mechanism that involves two successive steps of nucleation-induced polymerization.

## INTRODUCTION

The immune system provides protection from the environment and is critically important for multiple aspects of mammalian biology. It consists of an adaptive component that generates specific antibodies and cells through clonal selection, and an

innate component that utilizes preformed receptors. Innate immunity offers the first line of defense against infections and hazards by directly recognizing conserved pathogen- and danger-associated molecular patterns (PAMPs and DAMPs) to alert the immune system (Medzhitov and Janeway, 2000). Inflammasomes are key components of innate immunity inside the cell. They are formed in response to PAMPs and DAMPs and activate inflammatory caspases such as caspase-1 and -11 (Franchi et al., 2012; Lamkanfi and Dixit, 2012; Rathinam et al., 2012). Caspase activation can lead to proteolytic maturation of cytokines interleukin (IL)-1 $\beta$  and IL-18 and elicit the inflammatory form of cell death pyroptosis, as ways to control exogenous and endogenous invasions.

Inflammasomes are supramolecular assemblies composed of at least a sensor protein and a caspase and often the adaptor protein ASC. Based on the domain architecture of the sensor protein, inflammasomes may be divided into two families. The first family is known as ALR (Absent in Melanoma 2 [AIM2]-like receptor), named after the first identified member (Figure 1A). ALRs are composed of an N-terminal PYD and one or two HIN domains (Rathinam et al., 2012). AIM2 directly senses the cytosolic PAMPs double-stranded DNAs (dsDNAs), such as those associated with viruses, using its HIN domain (Jin et al., 2012; Rathinam et al., 2012). The second class of inflammasomes contains receptors in the NLR (nucleotide-binding domain [NBD] and leucine rich repeat [LRR]-containing receptors) family (Figure 1A). NBD belongs to the AAA+ superfamily of ATPase domains. Most NLRs contain an N-terminal PYD and are known as NLRPs. The best-studied NLRP3 inflammasome is activated following a wide range of pathogen and danger signals, including extracellular ATP and uric acid crystals (Franchi et al., 2012; Lamkanfi and Dixit, 2012; Rathinam et al., 2012). Upon activation, both AIM2 and NLRP3 recruit the PYD- and CARD-containing bipartite adaptor ASC (apoptosis-associated speck-like protein containing a CARD) through PYD/PYD interactions (Masumoto et al., 1999). ASC, in turn, recruits caspase-1 through CARD/CARD

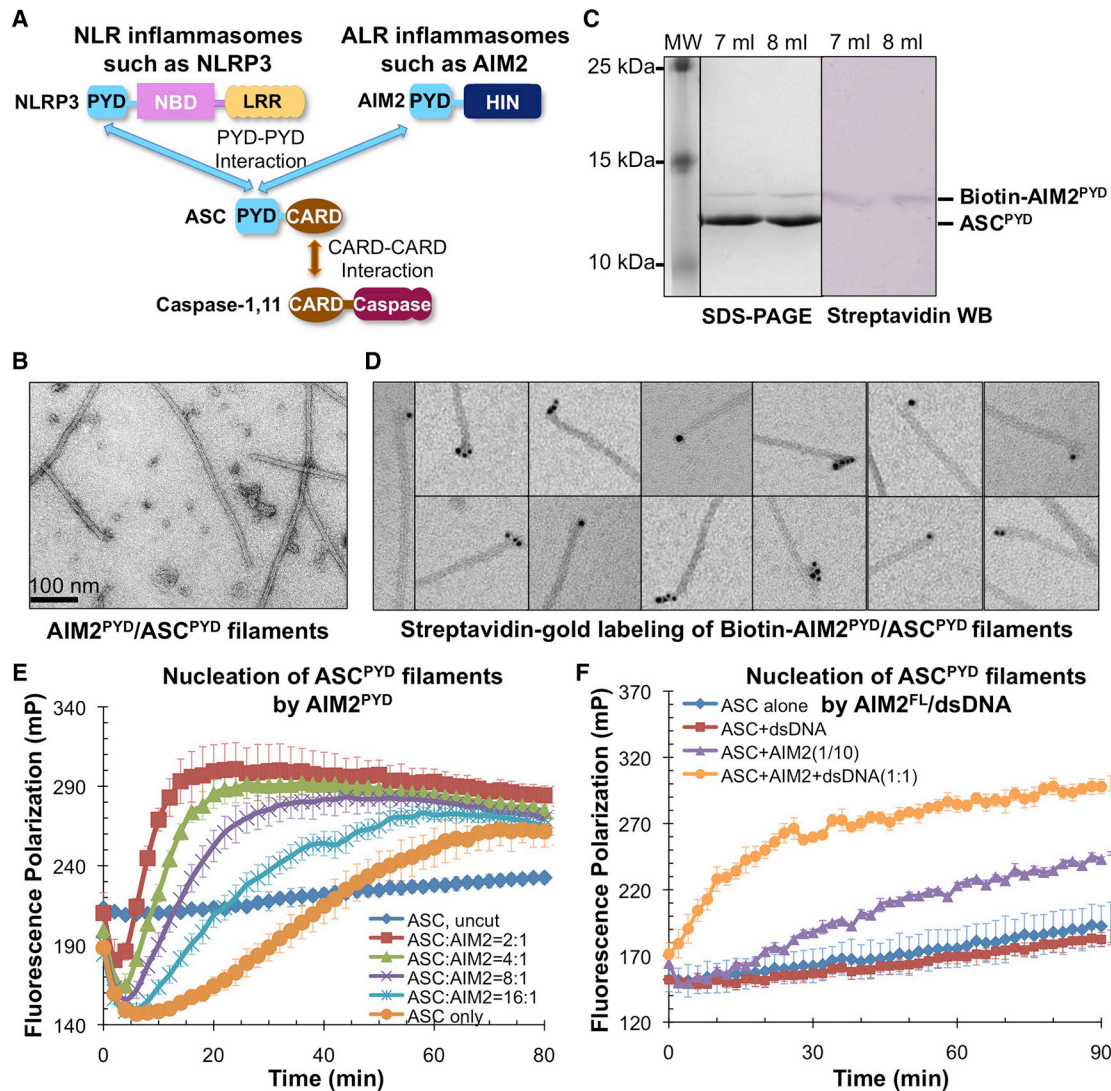


### Figure 1. AIM2 Promotes Formation of ASC<sup>PYD</sup> Filaments

(A) Domain composition and interaction hierarchy of NLRP3 and AIM2 inflammasomes.

(B) An electron micrograph of the AIM2<sup>PYD</sup>/ASC<sup>PYD</sup> binary complex.

(C) Gel filtration fractions of biotinylated AIM2<sup>PYD</sup>/ASC<sup>PYD</sup> complex as visualized by Coomassie-blue-stained SDS-PAGE (left) and streptavidin-alkaline phosphatase western blot (right). A lane between the marker and fraction samples on the SDS-PAGE was removed during figure preparation.

(D) Labeling of biotinylated AIM2<sup>PYD</sup>/ASC<sup>PYD</sup> binary complex by streptavidin-gold conjugate (6 nm).

(E) Fluorescence polarization (FP) assay of AIM2<sup>PYD</sup>-nucleated ASC<sup>PYD</sup> filament formation. mP, unit for FP. Data are represented as mean  $\pm$  SD ( $n = 3$ ).

(F) Effect of dsDNA on AIM2<sup>FL</sup>-nucleated ASC<sup>PYD</sup> filament formation. 2  $\mu$ M of AIM2<sup>FL</sup> monomer from gel filtration was incubated with or without equimolar 300 bp dsDNA (assuming a 10 bp footprint of AIM2 for molar calculation) for 30 min before diluting to a working concentration 0.1  $\mu$ M (ASC<sup>PYD</sup>: AIM2<sup>FL</sup> = 10:1) for the FP assay. Data are represented as mean  $\pm$  SD ( $n = 3$ ).

See also Figure S1.

interactions (Figure 1A). PYD and CARD both belong to the death domain (DD) fold superfamily (Ferraro and Wu, 2012), for which structures of two defined DD helical assemblies are known (Lin et al., 2010; Park et al., 2007).

Malfunctioning of inflammasomes is associated with serious human diseases (Strowig et al., 2012). Mutations in inflammasome proteins NLRP3, NLRP12, and MEFV (also known as Pyrin) are linked to autoinflammatory and fever syndromes (Rathinam et al., 2012). Aberrations in NLR inflammasome activation have

been connected to psoriasis, type II diabetes, inflammatory bowel diseases, and Alzheimer's disease (Franchi et al., 2012; Lamkanfi and Dixit, 2012; Rathinam et al., 2012; Strowig et al., 2012). The PYD-less ALR member, mouse p202, interacts with the HIN domain of AIM2 to inhibit inflammasome and potentiate lupus (Yin et al., 2013).

Immunofluorescence microscopy showed that transfected full-length ASC (ASC<sup>FL</sup>) and endogenous ASC upon stimulation both form speck-like aggregates (Masumoto et al., 1999).

Because transfected PYD and CARD-only ASC fragments are filamentous (Masumoto et al., 2001), the specks are most likely dense, crosslinked composites of PYD and CARD filaments. Because of the strong tendency of ASC to aggregate, the structures of ASC PYD (ASC<sup>PYD</sup>) and ASC<sup>FL</sup> were solved in monomeric states using nuclear magnetic resonance (NMR) at acidic conditions (de Alba, 2009; Liepinsh et al., 2003). Although additional monomeric PYD structures have been reported, including those of NLRP3 (Bae and Park, 2011) and AIM2 (Jin et al., 2013), the mode of homo- and hetero-PYD associations is entirely unknown.

Here, we used *in vitro* reconstitution, electron microscopy (EM) and polymerization assays to address assembly mechanisms for ASC-dependent AIM2 and NLRP3 inflammasomes. In contrast to the presumption that the different domain structures of AIM2 and NLRP3 may lead to considerable differences in the inflammasome architectures, we showed that both AIM2 upon dsDNA interaction and NLRP3 oligomerized through its NBD nucleate ASC<sup>PYD</sup> filaments. This is particularly surprising for NLRP3 due to the domain similarity of NLRs to Apaf-1-like molecules that form ring-like platforms (Yuan and Akey, 2013). The overarching paradigm had presumed that NLR inflammasomes are also ring-like structures. The flexibly linked ASC CARD (ASC<sup>CARD</sup>) then clusters along the ASC<sup>PYD</sup> filament to act as the platform for caspase-1<sup>CARD</sup> filament formation, leading to proximity-induced caspase dimerization and activation. The ternary inflammasome complex showed star-shaped branched filamentous morphology and exhibited unequal stoichiometries among the component proteins. We determined the cryoelectron microscopy (cryo-EM) structure of the ASC<sup>PYD</sup> filament at near-atomic resolution through helical reconstruction. The structure revealed molecular details of ASC<sup>PYD</sup>/ASC<sup>PYD</sup> interactions and allowed modeling of AIM2<sup>PYD</sup>/ASC<sup>PYD</sup> and NLRP3<sup>PYD</sup>/ASC<sup>PYD</sup> interactions. Structure-based mutagenesis confirmed the importance of ASC<sup>PYD</sup>/ASC<sup>PYD</sup>, AIM2<sup>PYD</sup>/ASC<sup>PYD</sup>, and NLRP3<sup>PYD</sup>/ASC<sup>PYD</sup> interactions *in vitro* and in cells. EM of immunoprecipitated endogenous NLRP3 inflammasome showed similar filamentous morphology as *in vitro*-reconstituted inflammasomes and quantitative western blotting confirmed the overstoichiometry of caspase-1 to ASC. Our studies collectively revealed a universal assembly process for ASC-dependent inflammasomes in both ALR and NLR families that involves nucleation-induced polymerization.

## RESULTS

### The AIM2<sup>PYD</sup>/ASC<sup>PYD</sup> Complex Is Filamentous with the End Location of AIM2<sup>PYD</sup>

To elucidate the assembly mechanisms for ASC-containing inflammasomes, we first reconstituted the interaction between AIM2 and ASC. Coexpression of AIM2<sup>PYD</sup> with ASC<sup>PYD</sup> showed that the complex eluted at the void position of a Superdex 200 gel filtration column (Figure S1A available online), suggesting formation of large “aggregates.” We used EM to visualize the negatively stained AIM2<sup>PYD</sup>/ASC<sup>PYD</sup> complex, which revealed filaments with uniform diameters of ~9 nm (Figure 1B).

AIM2<sup>PYD</sup> exists in substoichiometric molar ratio in the AIM2<sup>PYD</sup>/ASC<sup>PYD</sup> complex (Figures S1A and 1C). To understand

this observation, we generated a construct of AIM2<sup>PYD</sup> capable of enzymatic biotinylation during expression. Coexpression of the AIM2<sup>PYD</sup> construct with ASC<sup>PYD</sup> generated a complex with specific biotinylation of AIM2<sup>PYD</sup>, shown by streptavidin western blotting (Figure 1C). Labeling biotinylated AIM2<sup>PYD</sup> by 6 nm streptavidin-gold particles showed that AIM2<sup>PYD</sup> is localized at one end of the filaments (Figure 1D). The number of bound gold particles varies between one and several, consistent with the ability of AIM2<sup>PYD</sup> to form filaments when expressed alone (Figure S1B). In the presence of ASC<sup>PYD</sup>, AIM2<sup>PYD</sup> preferentially associated with ASC<sup>PYD</sup> to generate short heterogeneous AIM2<sup>PYD</sup> filaments in complex with much longer ASC<sup>PYD</sup> filaments. In contrast, Ni-NTA-gold labeling of His-tagged ASC<sup>PYD</sup> in the biotinylated AIM2<sup>PYD</sup>/ASC<sup>PYD</sup> complex showed uniform distribution along the filaments (Figure S1C), confirming that ASC<sup>PYD</sup> forms the main filament body.

### AIM2<sup>PYD</sup> and the Full-Length AIM2/dsDNA Complex Nucleate ASC<sup>PYD</sup> Filaments

The end labeling of AIM2<sup>PYD</sup> suggested its role as the nucleator for directional polymerization of ASC<sup>PYD</sup>. To quantitatively assess ASC<sup>PYD</sup> filament formation, we set up a fluorescence polarization (FP) assay *in vitro* using a His-MBP-ASC<sup>PYD</sup> fusion construct with an added C-terminal Cys for conjugating with Alexa 488 fluorophore. The large fusion tag MBP inhibited ASC<sup>PYD</sup> polymerization to enable His-MBP-ASC<sup>PYD</sup> to be expressed in the monomeric form (Figure S1D). Polymerization of Alexa-488-labeled monomeric ASC<sup>PYD</sup> was initiated by addition of the TEV protease to remove His-MBP from the fusion protein. The increase in FP, which indicates ASC<sup>PYD</sup> polymerization, was monitored as a function of time (Figure 1E). Although ASC<sup>PYD</sup> did polymerize on its own upon His-MBP removal, the rates of polymerization were dramatically enhanced in the presence of increasing amounts of substoichiometric AIM2<sup>PYD</sup> (1/16–1/2 molar ratios) (Figure 1E). The initial drop in FP corresponded with His-MBP removal by TEV and the decrease in size of ASC<sup>PYD</sup>. At 5 min after TEV addition, about 75% His-MBP was removed from the fusion protein (Figure S1E). The AIM2<sup>PYD</sup>/ASC<sup>PYD</sup> filaments generated from the polymerization assay (Figure S1F) showed similar morphology to the coexpressed complex (Figure 1B).

Full-length AIM2 (AIM2<sup>FL</sup>) is a cytosolic dsDNA sensor in which the interaction of its C-terminal HIN domain with dsDNA induces ASC recruitment and inflammasome formation. The PYD in AIM2 has been shown to interact with its HIN domain to provide autoinhibition in the absence of dsDNA binding (Jin et al., 2013). To reconstitute AIM2 inflammasome activation *in vitro*, we expressed AIM2<sup>FL</sup> as a His-MBP fusion. Purified His-MBP-AIM2<sup>FL</sup> was first incubated with equimolar 300 bp dsDNA (molar ratio calculated based on 10 bp footprint of AIM2 on dsDNA), followed by mixing with Alexa-488-labeled His-MBP-ASC<sup>PYD</sup>. TEV was added to remove His-MBP to initiate ASC<sup>PYD</sup> polymerization as monitored by FP (Figure 1F). A dramatic increase in FP was observed upon activation of AIM2<sup>FL</sup> by dsDNA, recapitulating the cellular event of inflammasome activation. These data suggest that overcome of autoinhibition and oligomerization of AIM2 by dsDNAs are crucial for inducing ASC<sup>PYD</sup> polymerization.

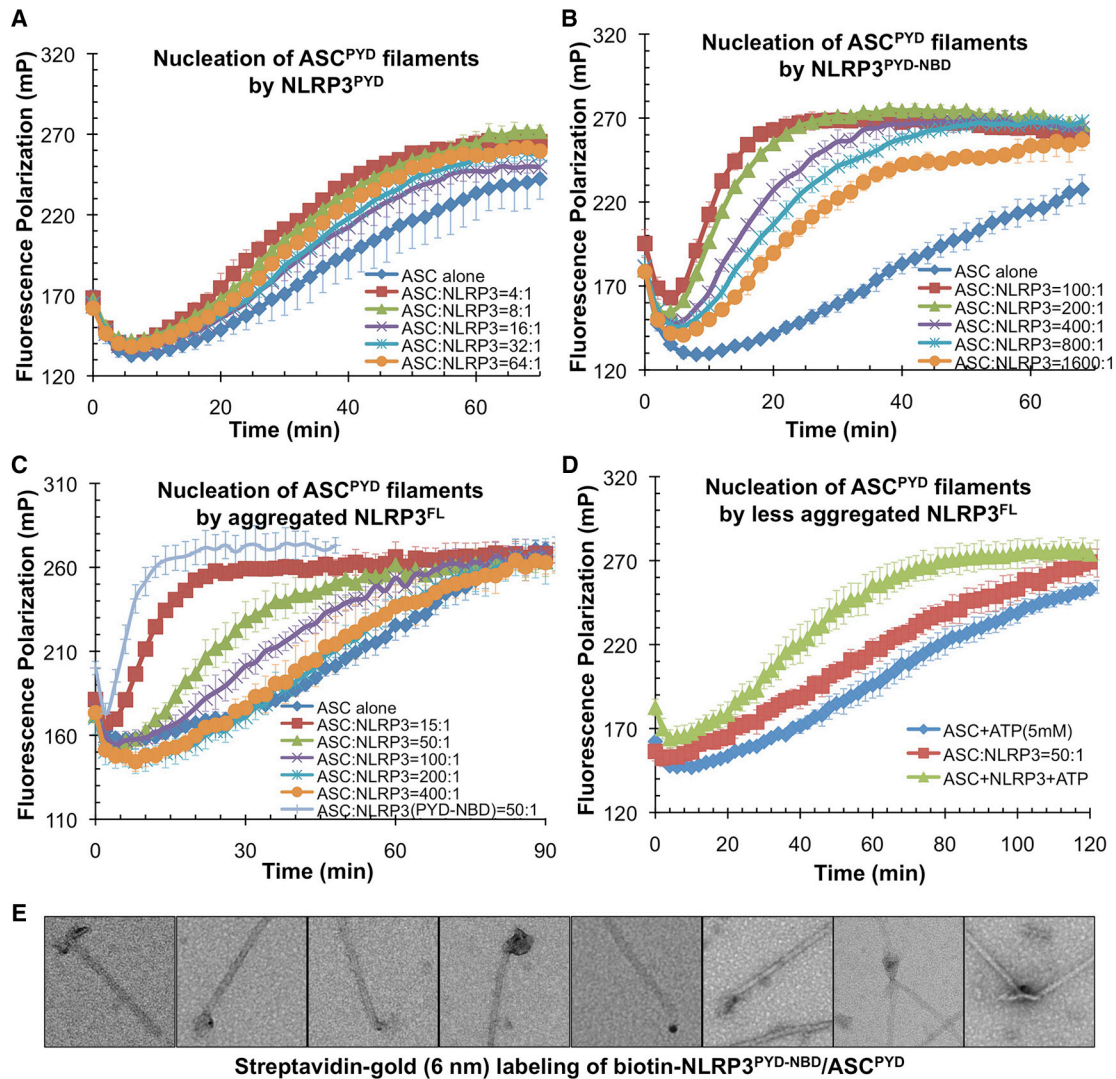


### Figure 2. NLRP3<sup>FL</sup> and NLRP3<sup>PYD-NBD</sup>, but Not NLRP3<sup>PYD</sup>, Promote ASC<sup>PYD</sup> Filament Formation

(A–C) Nucleation of ASC<sup>PYD</sup> filaments by titrating increasing amounts of NLRP3<sup>PYD</sup> (A), NLRP3<sup>PYD-NBD</sup> (B), NLRP3<sup>FL</sup> (C) as monitored by fluorescence polarization. Data are represented as mean  $\pm$  SD (n = 3).

(D) A less aggregated gel filtration fraction of NLRP3 was subjected to ASC<sup>PYD</sup> polymerization assay with or without 5 mM ATP. Data are represented as mean  $\pm$  SD (n = 3).

(E) Streptavidin-gold (6 nm) labeling of biotinylated NLRP3<sup>PYD-NBD</sup>/ASC<sup>PYD</sup> binary complex.

See also Figure S2.

### NLRP3<sup>PYD-NBD</sup> Nucleates and End Labels ASC<sup>PYD</sup> Filaments

NLRs share similar domain architectures and are recognized to be autoinhibited in the absence of suitable ligands. In NLRC4, an NLR with a CARD, its LRR domain plays an important role in inhibiting NLR oligomerization (Hu et al., 2013). Due to their domain similarity to Apaf-1-like molecules that form ring-like platforms through the NBDs to induce caspase activation and apoptosis (Yuan and Akey, 2013), the overarching paradigm appears to presume that NLRP inflammasomes are also ring-like structures organized by the NBD. Formation of filamentous structures in the AIM2<sup>PYD</sup>/ASC<sup>PYD</sup> interaction prompted us to

examine ASC-dependent NLRP inflammasomes using the prototypical member NLRP3.

We expressed and purified NLRP3<sup>PYD</sup>, NLRP3<sup>PYD-NBD</sup>, and NLRP3<sup>FL</sup>. Although AIM2<sup>PYD</sup> exists as filamentous oligomers and was sufficient in promoting ASC<sup>PYD</sup> polymerization, NLRP3<sup>PYD</sup> is a monomer and did not cause significant enhancement in ASC<sup>PYD</sup> polymerization (Figure 2A). Both insect cell and *E. coli* expressed NLRP3<sup>PYD-NBD</sup> with inclusion of the NBD eluted from the void position of a Superdex 200 gel filtration column and induced greatly increased ASC<sup>PYD</sup> polymerization (Figure 2B). In comparison, NLRP3<sup>PYD-NBD</sup> is a much stronger promoter of ASC<sup>PYD</sup> polymerization than AIM2<sup>PYD</sup>; it caused significant

enhancement of ASC<sup>PYD</sup> polymerization at a low 1:1,600 molar ratio (Figure 2B). Notably, under the physiological intracellular condition of 140 mM KCl and 10 mM NaCl (pH 7.4) and a lower ASC concentration, ASC<sup>PYD</sup> did not significantly polymerize unless increasing amounts of NLRP3<sup>PYD-NBD</sup> were added (Figure S2A), suggesting that ASC does not polymerize under steady physiological state without stimulation. The PYD of NLRP3 is required for ASC<sup>PYD</sup> polymerization because NLRP3<sup>PYD-NBD</sup> proteins with mutations on PYD are compromised in this function (see below), suggesting that NBD-oligomerized NLRP3<sup>PYD</sup> forms the platform for ASC<sup>PYD</sup> polymerization.

Insect-cell-expressed NLRP3<sup>FL</sup> showed a wide distribution on a Superdex 200 gel filtration column (Figure S2B). In keeping with autoinhibition in NLRP3<sup>FL</sup> as in NLRC4 (Hu et al., 2013), we found that even the highly aggregated NLRP3<sup>FL</sup> showed less activity than NLRP3<sup>PYD-NBD</sup> in promoting ASC<sup>PYD</sup> polymerization because more molar quantities of NLRP3<sup>FL</sup> were required to achieve similar degrees of FP enhancement (Figures 2B and 2C). Despite being activated by an extensive list of stimuli, it is uncertain what constitutes the direct activator of NLRP3 (Rathnam et al., 2012). We found that addition of ATP enhanced the less aggregated fractions of recombinant NLRP3<sup>FL</sup> in activating ASC<sup>PYD</sup> polymerization (Figure 2D); however, this activation is minimal in comparison. It is likely that ATP binding by the NBD is associated with, but not sufficient for, NLRP3 activation.

Induction of ASC<sup>PYD</sup> polymerization by NLRP3 suggests that NLRP3 may reside at the end of ASC<sup>PYD</sup> filaments. We generated a His-MBP-NLRP3<sup>PYD-NBD</sup> construct capable of enzymatic biotinylation during expression. We mixed purified His-MBP-NLRP3<sup>PYD-NBD</sup>-Biotin with His-MBP-ASC<sup>PYD</sup> and added the TEV protease to cleave off His-MBP to allow ASC<sup>PYD</sup> polymerization. The purified NLRP3-Biotin/ASC complex was subjected to negative-stain EM and 6 nm streptavidin-gold labeling, which confirmed localization of NLRP3 to the end of ASC<sup>PYD</sup> filaments (Figure 2E). Using negative-stain EM, we showed that purified NLRP3<sup>PYD-NBD</sup> is heterogeneous with a mixture of disk-like structures and filaments (Figure S2C). The latter may represent the spiral, lock washer-like mode of oligomerization of the NBD.

### Cryoelectron Microscopy Structure of ASC<sup>PYD</sup> at Near-Atomic Resolution

To generate a homogeneous population of ASC<sup>PYD</sup> filaments without the AIM2 or NLRP3 nucleators, we used *in vitro* ASC<sup>PYD</sup> polymerization starting from purified monomeric His-MBP-ASC<sup>PYD</sup> (Figure S1D). Upon TEV treatment to cleave off His-MBP, ASC<sup>PYD</sup> filaments spontaneously formed as shown by cryo-EM (Figure 3A). Cryo-EM images were collected using automated data acquisition on a Titan Krios with a Falcon II direct electron detector. Averaged power spectra of segments from cryo-EM images of the helical filaments showed a strong meridional reflection at  $1/13.9 \text{ \AA}^{-1}$ , which corresponds to the reciprocal of the axial rise but exhibited variable twist (Figures 3B and 3C), like many other helical polymers (Egelman et al., 1982). The magnitude of this variation can be seen in Movie S1.

Images were processed using the Iterative Helical Real Space Reconstruction (IHRSR) method with a solid cylinder as the initial reference (Egelman, 2000). The helical heterogeneity was dealt with by sorting images by twist to generate a subset with similar

helical parameters, resulting in a map at  $\sim 6 \text{ \AA}$  resolution. Correction of out-of-plane tilt was applied to further improve the map to a conservatively estimated resolution of  $\sim 3.8 \text{ \AA}$ , as determined by both Fourier shell correlation (FSC) (Rosenthal and Henderson, 2003) (Figure S3A) and comparison with the final atomic model (Figures S3B and S3C).

Rigid-body fitting of the NMR structure of ASC<sup>PYD</sup> (Liepinsh et al., 2003) into the cryo-EM map generated a pseudo atomic model of the ASC<sup>PYD</sup> filament. The fit of the NMR structure resolved the enantiomorphic ambiguity in EM reconstructions, but even without the NMR structure the hand of the  $\alpha$  helices in the reconstruction was clear, eliminating such ambiguities. The rigid-body fit was followed by real-space refinement (Schröder et al., 2007) to generate a final atomic model with clearly defined side chain densities (Figures 3D, 3E, and S3D). The ASC<sup>PYD</sup> filament is hollow with inner and outer diameters of  $\sim 20$  and  $\sim 90 \text{ \AA}$ , respectively (Figure 4A). The polar filament has a C3 point group symmetry with  $53^\circ$  right-handed rotation and  $14.0 \text{ \AA}$  axial rise per subunit, after correcting for a mean out-of-plane tilt of  $\sim 6^\circ$ .

The structure of ASC<sup>PYD</sup> in the filament exhibits conformational differences with that of ASC<sup>PYD</sup> alone (Figure 4B). This is apparent in the highly variable  $\alpha 2$ - $\alpha 3$  loop and the short  $\alpha 3$  helix, with clear cryo-EM density (Figure S4A). PYDs share a unique feature: the  $\alpha 3$  helix is shortened or missing and follows the long and flexible  $\alpha 2$ - $\alpha 3$  loop (Figure S4B). The conformational changes are likely due to participation of this region in all three types of interactions in the filament (see below and Figure S3D). Although the ASC<sup>PYD</sup> alone structure was determined at a pH below 4.0 (Liepinsh et al., 2003), lack of significant conformational differences elsewhere and absence of acidic residues in  $\alpha 3$  helix support the structural changes as due to filament formation. Among known PYD structures, NLRP3<sup>PYD</sup> and ASC2<sup>PYD</sup> possess a conformation similar to the filament conformation of ASC<sup>PYD</sup> (Figure 4C), suggesting that NLRP3<sup>PYD</sup> and ASC2<sup>PYD</sup> may be better interactors with ASC<sup>PYD</sup>. The former similarity may account for the high efficiency of NLRP3<sup>PYD-NBD</sup> in promoting ASC<sup>PYD</sup> polymerization (Figure 2B). ASC2 is a PYD only protein that is highly homologous to ASC<sup>PYD</sup> and has been shown to associate with ASC to modulate caspase-1 activation (Stehlik et al., 2003). If ASC2 can be incorporated into ASC<sup>PYD</sup> filaments but lacks the effector CARD, it could inhibit caspase-1 recruitment and activation. One face of a cross-section of the filament is largely negatively charged, whereas the opposite face is largely positively charged (Figure 4D), suggesting the role of charge complementarity in filament assembly.

### Detailed Interactions in the ASC<sup>PYD</sup> Filament

There are three major asymmetric interfaces (types I, II, and III) in the filament, one within each of the three-start helical strands (type I), and two between the strands (types II and III) (Figure 4E). Remarkably, despite being within the DD superfamily, the PYD/PYD interactions show remarkable differences to the DD complex structures (Figures 4F and S4C–S4E; Table S1). If one of the subunits is aligned, the corresponding partner subunit would need to rotate by  $15^\circ$ – $26^\circ$ ,  $21^\circ$ – $35^\circ$ , and  $18^\circ$ – $52^\circ$  for the type I, II, and III interfaces, respectively, relative to the corresponding interfaces in the MyD88/IRAK4/IRAK2 DD complex and the

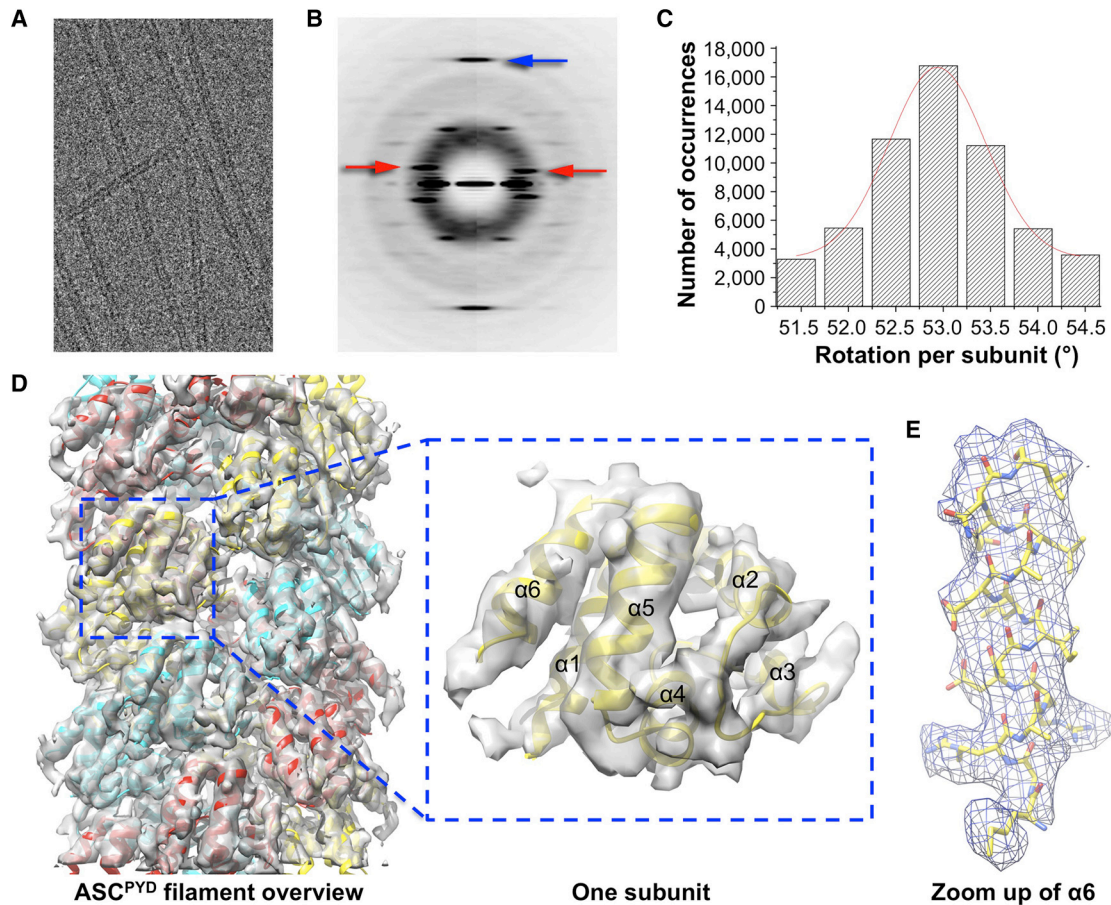


**Figure 3. Cryo-EM Structure of the ASC<sup>PYD</sup> Filament at Near-Atomic Resolution**

(A) A cryo-EM image of ASC<sup>PYD</sup> filaments.

(B) Average power spectra of ASC<sup>PYD</sup> filaments in two twist bins (left and right halves) showing constant axial rise per subunit (blue arrow) and variable long-range twist features (red arrows).

(C) Filament segments can be divided into separate twist bins according to azimuth angle, or rotation per subunit.

(D) Cryo-EM reconstruction of the ASC<sup>PYD</sup> filament, superimposed with the final atomic model shown in three colors each for one start of the three-start helical assembly.

(E) A zoom up view of helix  $\alpha 6$  shown in stick model and superimposed with the EM density.

See also [Figure S3](#) and [Movie S1](#).

PIDD/RAIDD DD complex (Ferrao and Wu, 2012; Lin et al., 2010; Park et al., 2007) (Figures S4C–S4E; Table S1). Relatively, the structural superposition indicates that the type I interaction is the most conserved, which is also the most dominant, burying about 880 Å<sup>2</sup> of surface area. Type II and III interactions are highly variable and bury 540 and 360 Å<sup>2</sup> of surface area, respectively. Structural differences between PYD and other members of the DD fold superfamily and formation of a substantial central cavity may have shifted the relative orientations of the subunits in the type I, II, and III interactions.

In the previously observed DD/DD interactions, type I is mediated by residues at  $\alpha 1$  and  $\alpha 4$  (type Ia) and residues at  $\alpha 2$  and  $\alpha 3$  (type Ib) (Ferrao and Wu, 2012; Lin et al., 2010; Park et al., 2007). Despite being the most conserved, the relative shift in orientation and the structural differences between DDs and PYDs minimized the involvement of  $\alpha 3$  in the intrastrand type I PYD/PYD interaction (Figures 4G and S3D). In the interstrand type II PYD/PYD

interaction, residues at the  $\alpha 4$ - $\alpha 5$  corner of one ASC<sup>PYD</sup> (type IIa) and residues at the  $\alpha 5$ - $\alpha 6$  corner of the second ASC<sup>PYD</sup> (type IIb) mediate this interaction (Figures 4H and S3D). In the interstrand type III PYD/PYD interaction,  $\alpha 2$ - $\alpha 3$  corner of one ASC<sup>PYD</sup> (type IIIa) interacts with the  $\alpha 1$ - $\alpha 2$  corner (type IIIb) of the other subunit (Figures 4I and S3D). Prominently, the PYD-unique and highly variable  $\alpha 2$ - $\alpha 3$  loop participates in all three types of PYD/PYD interactions (Figure S3D), which may explain the conformational changes in this region upon filament formation (Figure 4B). Overall the interactions contain charged, hydrophilic, and hydrophobic components, with charge interactions playing an important role (Figures S4F–S4H). Consistently, ASC<sup>PYD</sup> polymerization exhibits salt dependence (Figure S4I).

#### Structure-Based Mutagenesis In Vitro and in Cells

Structure-guided mutagenesis in vitro confirmed the role of type I, II, and III interactions in ASC<sup>PYD</sup> filament formation, as shown

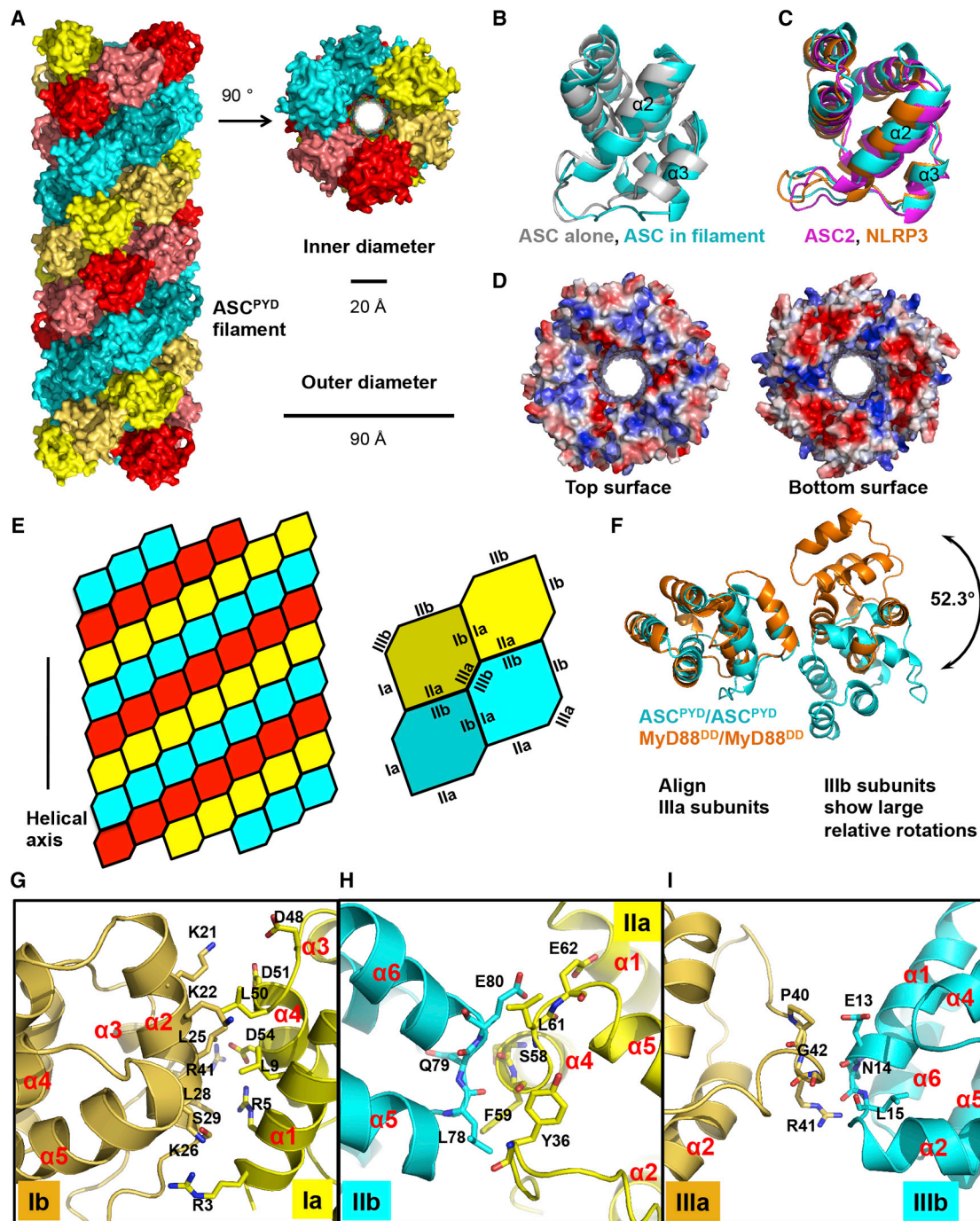


**Figure 4. Detailed Cryo-EM Model of the ASC<sup>PYD</sup> Filament**

(A) The ASC<sup>PYD</sup> filament is a three-start helical assembly with C3 symmetry as shown in a surface representation. The three-start helical strands are denoted by red, cyan, and yellow, respectively, with alternating darker and lighter shades to show subunit boundaries.

(B) Comparison of the initial ASC<sup>PYD</sup> subunit model (gray, PDB ID 1UCP) and the subunit structure after refinement against the cryo-EM density (cyan).

(C) Structures of ASC<sup>2PYD</sup> (magenta) and NLRP3<sup>PYD</sup> (orange) are similar to the ASC<sup>PYD</sup> subunit structure in the filament (cyan).

(D) Electrostatic surface representations of approximate cross-sections of the filament.

(E) A schematic diagram of the ASC<sup>PYD</sup> filament and the three types of asymmetric interactions, defined in accordance with the previously observed DD/DD interactions.

(F) Comparison of the type III interactions in the ASC<sup>PYD</sup> filament (cyan) and in the MyD88/IRAK4/IRAK2 DD complex (orange).

(G–I) Detailed interactions in type I, II, and III interfaces, respectively. Side chains of interfacial residues are shown as stick models and labeled.

See also Figure S4.

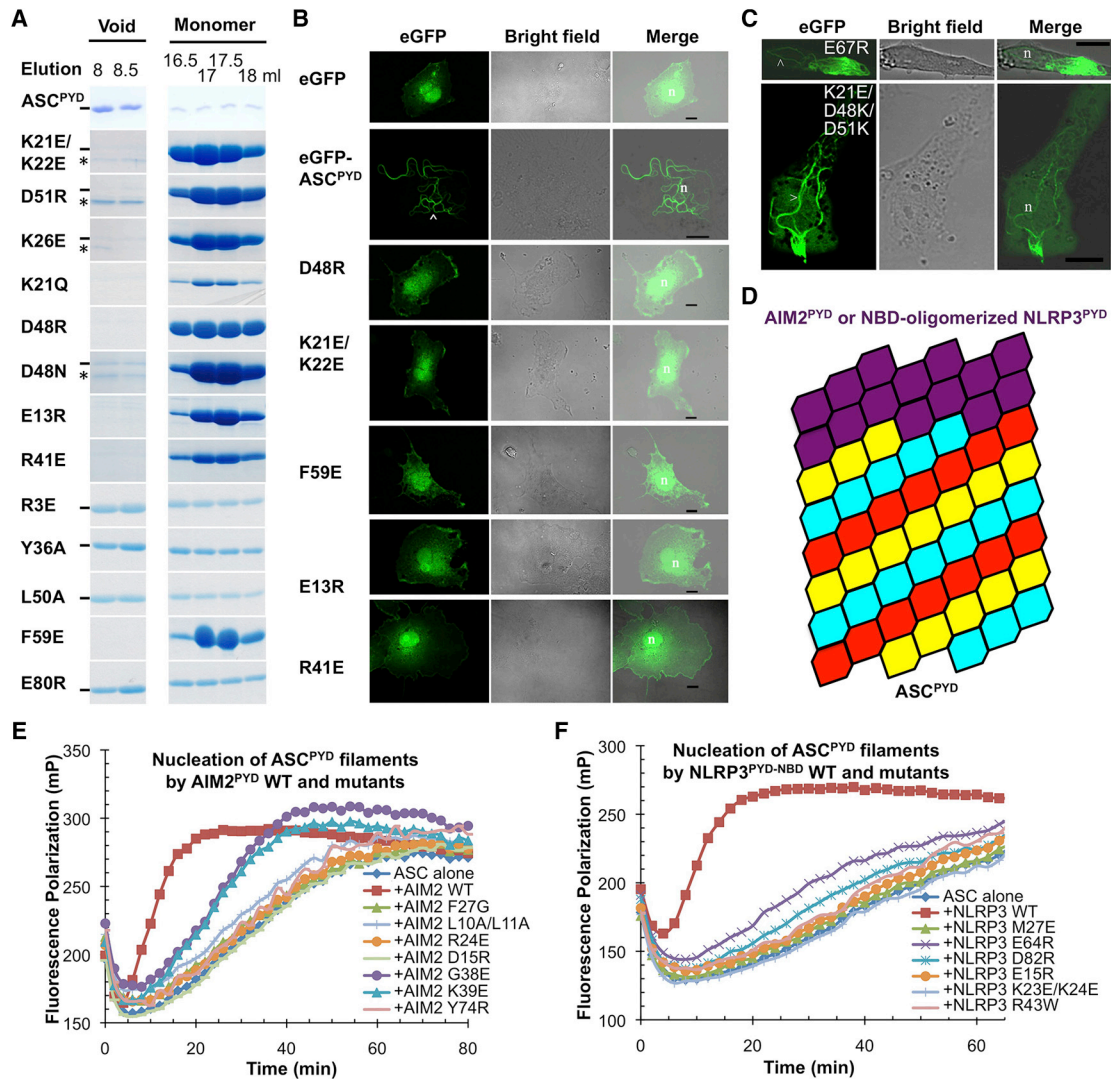


**Figure 5. Structure-Based Mutations Disrupt ASC<sup>PYD</sup> Filament Formation, AIM2<sup>PYD</sup>/ASC<sup>PYD</sup> Interaction, and NLRP3<sup>PYD</sup>/ASC<sup>PYD</sup> Interaction In Vitro and in Cells**

(A) Size-exclusion chromatography of WT and mutant ASC<sup>PYD</sup> showing both filamentous (void) and monomeric fractions from a Superdex 200 column. Hyphen denotes ASC<sup>PYD</sup> and asterisk denotes a contaminant.

(B) Morphology of transfected WT and mutant eGFP-tagged ASC<sup>PYD</sup> constructs visualized by confocal laser scanning microscopy. The arrowhead depicts filaments. n, nucleus; scale bars = 10  $\mu$ m.

(C) Morphology of transfected eGFP-tagged ASC<sup>PYD</sup> visualized by confocal laser scanning microscopy. Top: ASC<sup>PYD</sup> with charge reversal mutation on a residue outside the filament interface. Bottom: ASC<sup>PYD</sup> with triple-charge reversal mutation that rescued the defectiveness of the single mutants. Arrowheads depict filaments.

(D) A schematic model of AIM2<sup>PYD</sup>/ASC<sup>PYD</sup> or NLRP3<sup>PYD</sup>/ASC<sup>PYD</sup> filaments composed of a top AIM2<sup>PYD</sup> or NLRP3<sup>PYD</sup> layer extended by ASC<sup>PYD</sup> filament body.

(E and F) Mutations of conserved interfacial residues on AIM2<sup>PYD</sup> (E) and NLRP3<sup>PYD-NBD</sup> (F) reduced or abolished their ability to nucleate ASC<sup>PYD</sup> filaments. See also Figure S5.

by elution in more monomeric fractions (Figure 5A). In particular, K21Q, K21E/K22E, K26E, R41E, D48R, D48N, and D51R of the type I interface, F59E of the type II interface, and E13R and R41E of the type III interface abolished filament formation (Figure 5A; Table S2). Additional mutations, R3E and L50A of the type I interface, and Y36A and E80R of the type II interface, weakened filament formation as shown by increased presence in the monomeric fractions in comparison with the wild-type (WT) (Figure 5A; Table S2). Mutations that disrupted filament for-

mation in vitro also abrogated the ability of eGFP-ASC<sup>PYD</sup> to form filaments in cells as shown by confocal and fluorescence microscopy (Figures 5B, S5A, and S5B) and by EM of immunopurified samples (Figures S5C and S5D). A previous extensive mutagenesis study on surface-exposed charged residues confirmed the importance of additional observed interfacial residues in ASC<sup>PYD</sup> filament formation in cells (Moriya et al., 2005) (Table S2).

In contrast to disruptive phenotypes of mutations on interfacial residues, the charge reversal mutation E67R outside the

interface did not affect eGFP-ASC<sup>PYD</sup> filament formation (Figure 5C). At the type I interface, K21, D48, and D51 interact with each other (Figure 4G), and mutations on each of the residues disrupt filament formation (Figures 5A and 5B). Remarkably, the triple-charge reversal mutant K21E/D48K/D51K rescued eGFP-ASC<sup>PYD</sup> filament formation in cells (Figure 5C), supporting the validity of the structurally observed interactions.

### Modeled AIM2<sup>PYD</sup>/ASC<sup>PYD</sup> and NLRP3<sup>PYD-NBD</sup>/ASC<sup>PYD</sup> Interactions

The ASC<sup>PYD</sup> filament structure provides a template for modeling the AIM2<sup>PYD</sup>/ASC<sup>PYD</sup> and NLRP3<sup>PYD</sup>/ASC<sup>PYD</sup> hetero-PYD/PYD interactions using the published crystal structures of AIM2<sup>PYD</sup> (Jin et al., 2013) and NLRP3<sup>PYD</sup> (Bae and Park, 2011). End locations of AIM2<sup>PYD</sup> and NLRP3<sup>PYD</sup> in their complexes with ASC<sup>PYD</sup> filaments suggest that the PYDs in AIM2 and NLRP3 continue the helical arrangement seen in the ASC<sup>PYD</sup> filament using a combination of the same type I, II, and III interactions (Figure 5D). Given the observed conformational changes at the  $\alpha 2$ - $\alpha 3$  corner, which points down in the helical diagram (Figure 4D), we reasoned that AIM2 and NLRP3 PYDs should reside above the ASC<sup>PYD</sup> filament (Figure 5D).

We selected residues in AIM2<sup>PYD</sup> and NLRP3<sup>PYD</sup> structures corresponding to those in ASC<sup>PYD</sup> that caused impairment in filament formation when mutated (Figures 5A and 5B). Assaying the ability of AIM2<sup>PYD</sup> and NLRP3<sup>PYD-NBD</sup> mutants in promoting ASC<sup>PYD</sup> polymerization showed that mutations on each of the predicted interfaces in AIM2<sup>PYD</sup>, including L10A/L11A, R24E and F27G of the type I interface, Y74R of the type II interface, and G38E, K39E, and D15R of the type III interface, either abolished or showed greatly reduced promotion of ASC<sup>PYD</sup> polymerization (Figure 5E; Table S3). Additionally, in a recently published study on AIM2<sup>PYD</sup>, the D19A/E20A/E21A/D23A mutation, which harbors mostly type I interface residues, abolished the interaction with ASC<sup>PYD</sup> (Jin et al., 2013). Similarly, mutations at each of the predicted type I, II, and III interfacial residues on NLRP3<sup>PYD</sup>, including K23E/K24E and M27E of the type I interface, E64R and D82R of the type II interface, and R43W and E15R of the type III interface, caused almost complete impairment in promoting ASC<sup>PYD</sup> polymerization by the NLRP3<sup>PYD-NBD</sup> construct (Figure 5F; Table S3). It should be noted because AIM2<sup>PYD</sup> also aggregates into similar filaments (Figure S1B), the same mutations would likely affect both AIM2/ASC interaction and AIM2 self-association. For NLRP3, the PYD does not self-associate, whereas the NBD mediates self-association; therefore, the PYD mutations in NLRP3 would directly affect ASC interaction. Collectively, these data support that the interactions in the ASC<sup>PYD</sup> filament also define the mode of hetero-oligomerization in the AIM2<sup>PYD</sup>/ASC<sup>PYD</sup> and NLRP3<sup>PYD</sup>/ASC<sup>PYD</sup> interaction pairs.

### Reconstitution of the Ternary AIM2 Inflammasome

The C termini of ASC<sup>PYD</sup> subunits extend prominently outward from the filament (Figure 6A), providing a connection to the CARD in ASC after a 23-residue linker. Superposition of the NMR structure of ASC<sup>FL</sup> (de Alba, 2009) with ASC<sup>PYD</sup> in the filament displayed the flexibly linked, peripheral ASC<sup>CARD</sup> (Figure 6B). To reveal the structural architecture of full ternary inflammasomes, we expressed and purified His-GFP-caspase-1<sup>CARD</sup>,

His-MBP-ASC<sup>FL</sup>, and His-MBP-AIM2<sup>PYD</sup>. We mixed the three proteins with the TEV protease to allow His-MBP removal and formation of a ternary complex. His-tag pull-down showed that His-GFP-caspase-1<sup>CARD</sup> interacted with ASC<sup>FL</sup> and AIM2<sup>PYD</sup> (Figure 6C). The stoichiometry between ASC<sup>FL</sup> and AIM2<sup>PYD</sup> in the ternary complex is consistent with that in the AIM2<sup>PYD</sup>/ASC<sup>PYD</sup> binary complex with AIM2<sup>PYD</sup> under stoichiometric (Figure 1C). ASC, in turn, appeared under stoichiometric to caspase-1. EM showed that the ternary complex is star shaped (Figure 6D). Anti-ASC immunogold labeling (15 nm) showed that ASC resides in the center of the stars (Figure 6D). In contrast, Ni-NTA conjugated with 6 nm gold particles labeled His-GFP-caspase-1<sup>CARD</sup> along the arms of the stars (Figure 6E). These data suggest that AIM2<sup>PYD</sup> nucleates short filaments of ASC<sup>FL</sup> through PYD/PYD interactions and ASC<sup>CARD</sup> further initiates caspase-1<sup>CARD</sup> filaments to promote caspase-1 activation. Because the linker between ASC PYD and CARD is flexible, the outer CARDS should be able to cluster together and act as the platform for caspase-1 polymerization (Figure 6B).

We tested the role of ASC<sup>CARD</sup> in inflammasome assembly using a caspase-1<sup>CARD</sup> polymerization assay. We used “sandwich”-tagged His-MBP-caspase-1<sup>CARD</sup>-Sumo construct because N-terminally tagged His-MBP-caspase-1<sup>CARD</sup> construct still formed filaments. A sortase motif was added for fluorophore labeling (Theile et al., 2013). Polymerization of caspase-1<sup>CARD</sup> was initiated by addition of TEV to cleave off His-MBP and monitored by fluorescence polarization. In the presence ASC<sup>FL</sup> or ASC<sup>CARD</sup> at substoichiometric ratios, caspase-1<sup>CARD</sup> polymerization was greatly enhanced (Figure 6F), consistent with nucleation of caspase-1 polymerization by ASC.

It is intriguing that the ASC<sup>FL</sup> component in the ternary complex does not display as long filaments as it does in the binary AIM2<sup>PYD</sup>/ASC<sup>PYD</sup> or NLRP3<sup>PYD-NBD</sup>/ASC<sup>PYD</sup> complexes. We reasoned that because His-MBP-ASC<sup>FL</sup> forms bundled clusters minutes after removal of the His-MBP tag (Figure S6A) and precipitates, likely due to the CARD and its potential to crosslink filaments, ASC<sup>FL</sup> might only exist as short filaments such that almost all ASC<sup>CARD</sup> molecules are in complex with caspase-1<sup>CARD</sup>. To determine whether the same ASC<sup>PYD</sup> interactions in the observed filament govern those in the context of ASC<sup>FL</sup>, we cotransfected Myc-His-tagged ASC<sup>FL</sup> with WT and mutant ASC<sup>PYD</sup>-eGFP in 293T cells. Immunoprecipitated with anti-His antibody followed by anti-eGFP western showed that Myc-His-ASC<sup>FL</sup> pulled down WT ASC<sup>PYD</sup>-eGFP, but was severely impaired in interacting with ASC<sup>PYD</sup>-eGFP that harbors mutations on residues important for the ASC<sup>PYD</sup> filament formation (Figures 6G and S6B). We further tested the effects of PYD mutations in ASC<sup>FL</sup> using the in vitro inflammasome reconstitution assay. His-GFP-caspase-1<sup>CARD</sup> pulled down AIM2<sup>PYD</sup> in the presence of WT ASC<sup>FL</sup>, but not mutant ASC<sup>FL</sup> defective in formation of PYD filaments (Figure S6C), demonstrating that the same interactions in the PYD filaments govern the interaction in the ternary inflammasome complex.

### Morphology and Stoichiometry of Endogenous NLRP3 Inflammasome

Our data suggest a unified model of inflammasome assembly in which AIM2 upon dsDNA interaction or NLRP3 upon activation

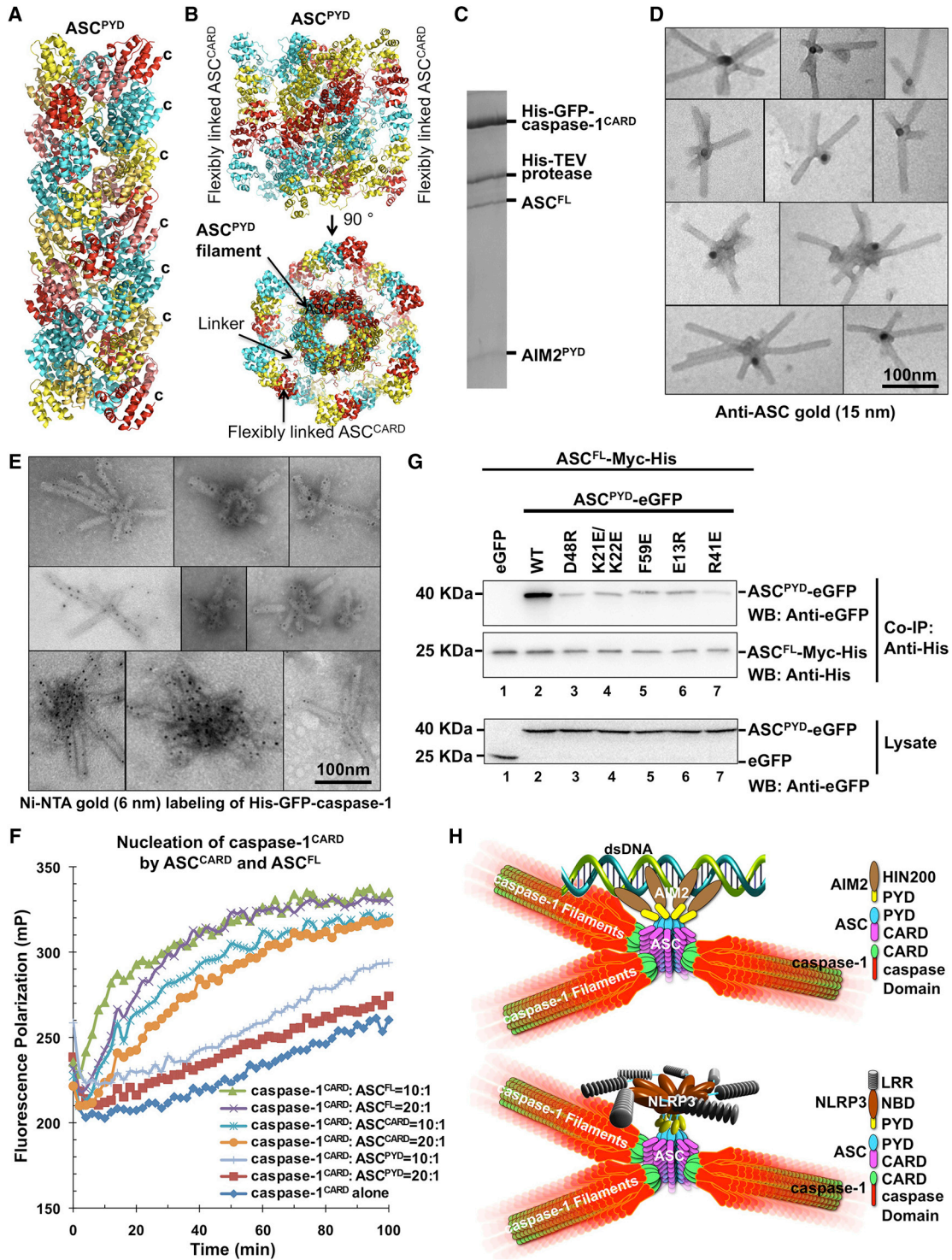


**Figure 6. Reconstitution of the Full Ternary AIM2 Inflammasome**

(A) The ASC<sup>PYD</sup> filament structure in a ribbon representation. The protruding C termini for connecting to ASC<sup>CARD</sup> are labeled for the subunits at the right. (B) ASC<sup>FL</sup> NMR structure (PDB ID 2KN6) is superimposed on the ASC<sup>PYD</sup> model to show the outward located ASC<sup>CARD</sup>. (C) Pull-down of the core AIM2 inflammasome in vitro as visualized on Coomassie-blue-stained SDS-PAGE. (D and E) Electron micrographs of His-GFP-caspase-1<sup>CARD</sup>/ASC<sup>FL</sup>/AIM2<sup>PYD</sup> ternary complex labeled with anti-ASC gold (D) and Ni-NTA gold (E). (F) Promotion of His-MBP-caspase-1<sup>CARD</sup>-Sumo (3 μM) polymerization by ASC<sup>FL</sup> or ASC<sup>CARD</sup> at substoichiometric ratios of 1:20 and 1:10 upon removal of His-MBP by TEV. ASC<sup>PYD</sup> did not enhance caspase-1<sup>CARD</sup> polymerization.

(legend continued on next page)

nucleates ASC helical clusters through PYD/PYD interactions (Figure 6H). The oligomerized ASC CARDs then form the platform for caspase-1<sup>CARD</sup> to nucleate into filaments, which, in turn, bring caspase domains into proximity for dimerization, *trans*-autocleavage, and activation (Figure 6H). To elucidate the morphology of endogenous inflammasomes, we stimulated THP-1 cells with uric acid crystals, immunoprecipitated the activated NLRP3 inflammasome using anti-ASC antibody, and subjected the immunoprecipitated sample to negative-stain EM. The images contained both single filaments (Figure 7A) and intertwined filaments (Figure S7A); the former resembles subcomplexes of in-vitro-reconstituted inflammasomes, and the latter resembles clustered, ball-of-yarn-like reconstituted inflammasomes that form upon overnight incubation (Figure S7B).

It has been shown previously that, upon stimulation, each cell forms one gigantic NLRP3 punctum adjacent to the nucleus (Fernandes-Alnemri et al., 2007). To visualize the structure of such a punctum in situ, we expressed ASC-eGFP in COS-1 cells and performed immunogold EM on ultrathin cryosections that preserve native structures. Control cells transfected with eGFP alone showed neither punctum nor anti-ASC gold labeling, and ASC-eGFP-transfected cells did not exhibit gold labeling in the absence of the anti-ASC primary antibody (Figure S7C). Specific gold labeling was shown in ASC-eGFP-transfected cells in the presence of anti-ASC primary antibody and protein A-gold (10 nm) treatment (Figure 7B). The labeling revealed a densely packed perinuclear punctum of about 2  $\mu\text{m}$  in size, in contrast to the hollow structure implicated previously (Masumoto et al., 1999). The dense structures are consistent with the ball-of-yarn-like architectures of in-vitro-reconstituted and in-cell-immunoprecipitated inflammasomes.

In vitro reconstitution of the ternary inflammasome suggests an overstoichiometry of caspase-1 to ASC (Figure 6C). To determine whether endogenous ASC-dependent inflammasomes from cells also possess the similar property, we stimulated THP-1 cells with uric acid crystals, immunoprecipitated the activated NLRP3 inflammasome using anti-ASC antibody, and performed quantitative western blotting using recombinant caspase-1 and ASC as standards. These experiments showed that caspase-1 is overstoichiometric to ASC, by  $\sim 3.5$ -fold in the current experiment (Figures 7C, 7D, S7D, and S7E). It should be noted that an anti-ASC antibody would have precipitated both ASC alone and its complex with caspase-1, and therefore, the measured 3.5-fold overstoichiometry should be an underestimation.

### Structure-Guided PYD Mutations Compromise IL-1 $\beta$ Processing

One main biological consequence of inflammasome activation is the processing of pro-IL-1 $\beta$  by caspase-1 to IL-1 $\beta$ . To address the consequence of structure-based mutations in biological

function, we used a cotransfection strategy to assay IL-1 $\beta$  processing (Jin et al., 2012). Cotransfection of caspase-1, pro-IL-1 $\beta$ , and ASC did not cause significant cleavage of pro-IL-1 $\beta$  into mature IL-1 $\beta$  (Figure 7E). Although addition of WT AIM2 activated the inflammasome and led to IL-1 $\beta$  production, cotransfection of PYD-interaction-defective AIM2 mutants compromised IL-1 $\beta$  conversion (Figure 7E), demonstrating the functional consequence of observed PYD/PYD interactions.

## DISCUSSION

### A Near-Atomic Resolution Structure by Cryo-EM

Our reconstruction of a small, structurally variable biological sample represents a significant advance in high-resolution structure determination by cryo-EM, made possible by automated microscopy (Potter et al., 1999), a state-of-the-art electron microscope (the Titan Krios), and a new generation of direct electron detectors (Bai et al., 2013; Bammes et al., 2012; Li et al., 2013; Liao et al., 2013), combined with existing computational approaches for variable twist polymers (Egelman, 2000; Egelman et al., 1982). Most of the structures that have been currently solved by cryo-EM to near-atomic resolution are icosahedral viruses that are highly ordered and with a high degree of internal symmetry (Zhou, 2011). In the absence of any mechanism to maintain long-range order, all biological polymers will display cumulative disorder (Egelman and DeRosier, 1982). We think that the new hardware and software advances in cryo-EM will have an enormous impact in allowing many biological polymers, including those whose helical symmetry could not even be determined with confidence, to now be reconstructed at near-atomic resolution.

### PYD/PYD Interactions

The ASC<sup>PYD</sup> filament structure presented here provides insights into molecular mechanisms of homo- and hetero-PYD associations in inflammasomes. Among the PYDs with known structures, NLRP3, NLRP12, AIM2, and ASC2 have been shown to interact with ASC (Rathinam et al., 2012; Stehlik et al., 2003). Consistently, they exhibit the highest sequence conservation at the ASC-interaction surfaces with 61%, 54%, 50%, and 89% homology, respectively (Table S4). The ASC<sup>PYD</sup> structure may also provide a template for other PYDs with no structures such as the IFI16<sup>PYD</sup> filament cooperatively assembled on dsDNA (Morrone et al., 2013).

A number of mutations in NLRP3, NLRP12, and MEFV have been shown to associate with hereditary periodic fever syndromes. For NLRP3, all mutations are dominant and likely cause activation by overcoming autoinhibition (Touitou et al., 2004). For NLRP12, a nonsense mutation and a splicing defect generate truncated proteins at residues 284 and 646, respectively, and cause spontaneous inflammation (Jéru et al., 2008), suggesting

(G) Mutations in ASC<sup>PYD</sup> reduced its binding to ASC<sup>FL</sup>. ASC<sup>FL</sup>-Myc-His was cotransfected with WT and mutant ASC<sup>PYD</sup>-eGFP. Immunoprecipitation and western blotting was carried out using anti-His and anti-eGFP antibodies, respectively.

(H) Model of inflammasome assembly. Upstream sensing proteins such as AIM2 and NLRP3 oligomerize upon activation to form a platform of PYDs that induces ASC filament assembly through PYD/PYD interactions. Multiple ASC<sup>CARD</sup> molecules cluster to promote caspase-1 filament formation through CARD/CARD interactions. Proximity induced dimerization of the caspase domain activates the enzyme followed by autocleavage.

See also Figure S6.

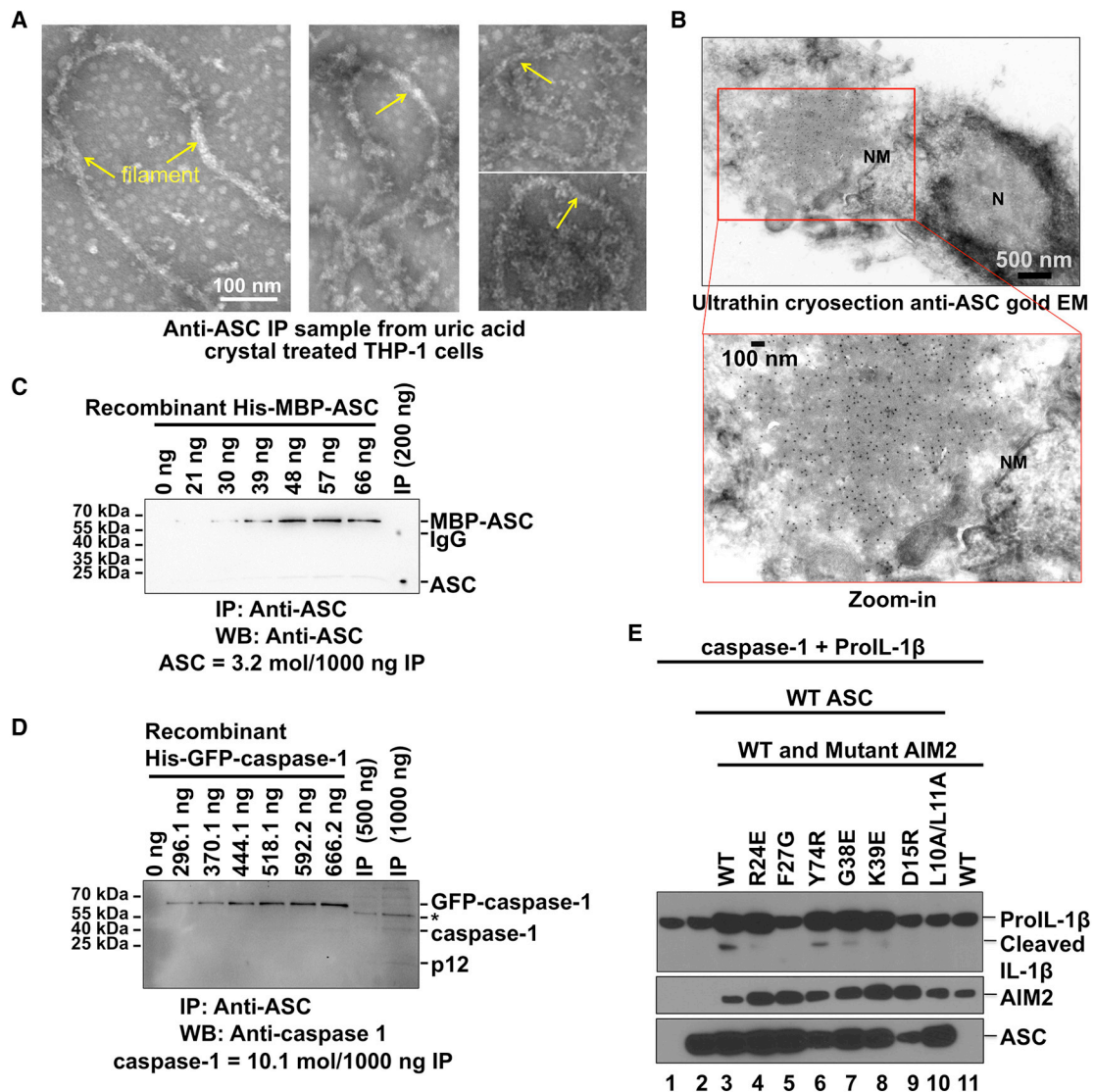


**Figure 7. Morphology, Stoichiometry, and Pro-IL-1 $\beta$  Processing in Inflammasomes**

(A) Morphology of anti-ASC-immunoprecipitated NLRP3 inflammasomes from uric-acid-crystal-activated THP-1 cells analyzed by negative-stain EM. Arrows denote filaments.

(B) Immunogold EM on ultrathin cryosections from ASC<sup>FL</sup>-eGFP-transfected COS-1 cells. The ASC-containing compact structure is densely decorated by gold particles (10 nm). N, nucleus; NM, nuclear membrane.

(C and D) Quantification of immunoprecipitated ASC-containing complex (IP) from uric-acid-crystal-activated THP-1 cells using quantitative anti-ASC (C) and anti-caspase-1 p12 (D) western blotting. Known amounts of recombinant His-MBP-ASC and His-GFP-caspase-1 were western blotted to generate standard curves. The full-length caspase-1 and the cleaved p12 bands were both included in the quantification. The asterisk denotes IgG.

(E) AIM2 inflammasome reconstitution in HEK293T cells to define the functional consequence of structure-based mutations in AIM2. Cells were cotransfected with plasmids encoding pro-IL-1 $\beta$  and caspase-1 (lane 1), plus ASC alone (lane 2), or WT AIM2 alone (lane 11), or ASC together with WT or indicated AIM2 mutants (lanes 3–10). Maturation of pro-IL-1 $\beta$  into biologically active IL-1 $\beta$  was detected by western blotting using anti-IL-1 $\beta$  antibody (top). The expression levels of HA-ASC and Flag-AIM2 were detected by western blotting using anti-HA and anti-Flag antibodies (bottom).

See also Figure S7.

that the PYD and part of the NBD are sufficient for inflammasome formation and activation. For MEFV, hundreds of variants, most of which are associated with Familial Mediterranean Fever (FMF), have been identified (Touitou et al., 2004). Gene insertion “knockin” (KI) mouse models with three frequent FMF-associated mutations (M680I, M694V, and V726A) showed that they

caused severe spontaneous inflammatory phenotypes (Chae et al., 2011). Most relevant to the PYD interactions, six mutants, T12I, Y19C, K25R, R39G, E84K, and A89T, have been mapped to the PYD of MEFV (Touitou et al., 2004). None of these residues directly map to the PYD/PYD interaction surfaces (Figure S3D) and may therefore act by overcoming autoinhibition.

## A Unified Assembly Mechanism for Inflammasomes

Our data here present a mechanism for the assembly of ASC-dependent inflammasomes, in which AIM2 and NLRP3 both nucleate helical ASC clusters through PYD/PYD interactions, and ASC, in turn, nucleates caspase-1 filaments through CARD/CARD interactions (Figure 6H). These minimal structures coalesce to form the micron-sized, dense structures we observed in situ. We propose that CARD-containing NLRs (NLRs), which are independent of ASC, may also form filamentous structures by directly promoting caspase-1 polymerization through CARD/CARD interactions. Therefore, the mechanism of nucleation-induced filament formation may extend beyond ASC-dependent inflammasomes. It has been shown that uncleaved caspase-1 catalytic domain forms dimers in crystals (Elliott et al., 2009); this dimerization may occur within caspase-1 filaments in inflammasomes, resulting in intradimer cleavage, stabilization of dimerization, and enhancement of enzymatic activity.

Recent studies have revealed that in many innate immune pathways, multiple intracellular signaling proteins assemble into higher-order signaling machines for transmission of receptor activation information to cellular responses, with implicated new molecular mechanisms for threshold behavior, time delay of activation, and temporal and spatial control of signal transduction (Wu, 2013). Here, we show that inflammasomes also assemble into higher-order signalosomes that likely impart similar properties to its activation and kinetics. In this scenario, upon reaching the NLRP3 or AIM2 activation threshold, caspase-1 may polymerize until its concentrations falls below the dissociation constant. Given that caspase-1 is overstoichiometric to ASC by just a few fold, the average lengths of individual ASC-nucleated caspase-1 filaments in cells may be shorter than those reconstituted in vitro, leading to punctate, rather than filamentous morphology of intact inflammasomes. Once formed, inflammasomes may require active processes such as autophagy for their degradation (Saitoh et al., 2008). This scenario is reminiscent of the case for the filamentous CARMA1/Bcl10/MALT1 signalosome (Qiao et al., 2013) and may represent a general mechanism of disassembly of higher-order signalosomes in innate immunity to terminate signaling.

## EXPERIMENTAL PROCEDURES

### Recombinant Protein Expression and Purification

Various His-, His-MBP-, and His-MBP-Sumo “sandwich”-tag fusion constructs or coexpression constructs of AIM2, ASC, caspase-1, and NLRP3 were expressed in *E. coli* and insect cells. Biotinylation was performed in *E. coli* by coexpression with biotin ligase. All mutations in this construct were introduced using the QuikChange mutagenesis protocol.

### Polymerization Assays

His-MBP-ASC<sup>PYD</sup> and His-MBP-caspase-1<sup>CARD</sup>-Sumo were labeled with Alexa 488 and TAMRA fluorophores, respectively. Filament formation was monitored using fluorescence polarization upon addition of TEV protease to remove His-MBP, in the presence and absence of various nucleators of polymerization.

### Nanogold and Immunogold EM

Standard protocols were used for streptavidin-gold labeling of biotinylated proteins. Ni-NTA-nanogold labeling of His-tagged proteins, and immunogold labeling by appropriate antibodies using negative-stain EM. ASC-transfected

COS-1 cells were pelleted, fixed, flash frozen, and ultrathin sectioned for immunogold EM and contrasting with uranyl acetate.

### Cryo-EM, Image Processing, and Refinement

Grids containing ASC<sup>PYD</sup> were imaged using an FEI Titan Krios electron microscope operating at 300 keV, and recorded using a 4k × 4k Falcon II direct electron detector with a backthinned CMOS chip. The images were processed with SPIDER (Frank et al., 1996), and the IHRSR algorithm (Egelman, 2000) was used for helical reconstruction. The ASC<sup>PYD</sup> NMR structure (Protein Data Bank [PDB] ID 1UCP) (Liepinsh et al., 2003) was chosen as the starting model and the refinement was carried out using DireX (Schröder et al., 2007). We estimate the resolution of the reconstruction at ~3.8 Å as determined by both Fourier shell correlation and comparison with the final atomic model.

### AIM2 Inflammasome Reconstitution

HEK293T cells were transfected with pEFBOS-C-term-Guassia luciferase/Flag pro-IL-1β (~54 kDa), procaspase-1, HA-ASC, and the full-length wild-type or mutant Flag-AIM2 expression constructs using GeneJuice (Novagen). Cell lysates were probed with mouse anti-IL-1β monoclonal antibody. Expression of ASC and AIM2 was detected using anti-Flag and anti-HA antibodies, respectively. See also Extended Experimental Procedures.

### ACCESSION NUMBERS

The cryo-EM map of ASC<sup>PYD</sup> filament was deposited in EMDDataBank under accession code EMD-5830. The corresponding refined structure of ASC<sup>PYD</sup> in the filament was deposited in the Protein Data Bank with ID 3J63.

### SUPPLEMENTAL INFORMATION

Supplemental Information includes Extended Experimental Procedures, seven figures, four tables, and one movie and can be found with this article online at <http://dx.doi.org/10.1016/j.cell.2014.02.008>.

### AUTHOR CONTRIBUTIONS

A.L. performed in vitro reconstitution, electron microscopy on reconstituted samples, and polymerization assays, including Figures 1, 2, 5D–5F, 6C–6F, 6H, S1, S2, S4I, S6A, S6C, and S7B. V.G.M. performed confocal microscopy, cellular electron microscopy, immunoprecipitation, and western blotting, including Figures 5B, 5C, 6G, 7A–7D, S5, S6B, S7A, and S7C–S7E. J.R. performed structural analysis, refinement, and structure-based mutagenesis in vitro, including Figures 3D, 3E, 4, 5A, 6A, 6B, part of S3B, S3D, and S4A–S4H.

### ACKNOWLEDGMENTS

We thank Natacha Opalka, Seth Darst, Leona Cohen-Gould, Maria Ericsson, William Rice, and Mariena Silvestry Ramos for help with EM imaging, Harry Leung for help with confocal microscopy, Gabriel Nuñez for providing cDNAs, and the National Institutes of Health for funding support (AI050872 to H.W., EB001567 to E.H.E., and AI083713 to K.A.F.).

Received: October 6, 2013

Revised: December 4, 2013

Accepted: February 3, 2014

Published: March 13, 2014

### REFERENCES

- Bae, J.Y., and Park, H.H. (2011). Crystal structure of NALP3 protein pyrin domain (PYD) and its implications in inflammasome assembly. *J. Biol. Chem.* 286, 39528–39536.
- Bai, X.C., Fernandez, I.S., McMullan, G., and Scheres, S.H. (2013). Ribosome structures to near-atomic resolution from thirty thousand cryo-EM particles. *Elife* 2, e00461.

- Bammes, B.E., Rochat, R.H., Jakana, J., Chen, D.H., and Chiu, W. (2012). Direct electron detection yields cryo-EM reconstructions at resolutions beyond 3/4 Nyquist frequency. *J. Struct. Biol.* *177*, 589–601.
- Chae, J.J., Cho, Y.H., Lee, G.S., Cheng, J., Liu, P.P., Feigenbaum, L., Katz, S.I., and Kastner, D.L. (2011). Gain-of-function Pyrin mutations induce NLRP3 protein-independent interleukin-1 $\beta$  activation and severe autoinflammation in mice. *Immunity* *34*, 755–768.
- de Alba, E. (2009). Structure and interdomain dynamics of apoptosis-associated speck-like protein containing a CARD (ASC). *J. Biol. Chem.* *284*, 32932–32941.
- Egelman, E.H. (2000). A robust algorithm for the reconstruction of helical filaments using single-particle methods. *Ultramicroscopy* *85*, 225–234.
- Egelman, E.H., and DeRosier, D.J. (1982). The Fourier transform of actin and other helical systems with cumulative random angular disorder. *Acta Crystallogr. A* *38*, 796–799.
- Egelman, E.H., Francis, N., and DeRosier, D.J. (1982). F-actin is a helix with a random variable twist. *Nature* *298*, 131–135.
- Elliott, J.M., Rouge, L., Wiesmann, C., and Scheer, J.M. (2009). Crystal structure of procaspase-1 zymogen domain reveals insight into inflammatory caspase autoactivation. *J. Biol. Chem.* *284*, 6546–6553.
- Fernandes-Alnemri, T., Wu, J., Yu, J.W., Datta, P., Miller, B., Jankowski, W., Rosenberg, S., Zhang, J., and Alnemri, E.S. (2007). The pyroptosome: a supra-molecular assembly of ASC dimers mediating inflammatory cell death via caspase-1 activation. *Cell Death Differ.* *14*, 1590–1604.
- Ferrao, R., and Wu, H. (2012). Helical assembly in the death domain (DD) superfamily. *Curr. Opin. Struct. Biol.* *22*, 241–247.
- Franchi, L., Muñoz-Planillo, R., and Núñez, G. (2012). Sensing and reacting to microbes through the inflammasomes. *Nat. Immunol.* *13*, 325–332.
- Frank, J., Radermacher, M., Penczek, P., Zhu, J., Li, Y., Ladjadj, M., and Leith, A. (1996). SPIDER and WEB: processing and visualization of images in 3D electron microscopy and related fields. *J. Struct. Biol.* *116*, 190–199.
- Hu, Z., Yan, C., Liu, P., Huang, Z., Ma, R., Zhang, C., Wang, R., Zhang, Y., Martinon, F., Miao, D., et al. (2013). Crystal structure of NLRC4 reveals its auto-inhibition mechanism. *Science* *341*, 172–175.
- Jéru, I., Duquesnoy, P., Fernandes-Alnemri, T., Cochet, E., Yu, J.W., Lackmeyer-Port-Lis, M., Grimpel, E., Landman-Parker, J., Hentgen, V., Marlin, S., et al. (2008). Mutations in NALP12 cause hereditary periodic fever syndromes. *Proc. Natl. Acad. Sci. USA* *105*, 1614–1619.
- Jin, T., Perry, A., Jiang, J., Smith, P., Curry, J.A., Unterholzner, L., Jiang, Z., Horvath, G., Rathinam, V.A., Johnstone, R.W., et al. (2012). Structures of the HIN domain:DNA complexes reveal ligand binding and activation mechanisms of the AIM2 inflammasome and IFI16 receptor. *Immunity* *36*, 561–571.
- Jin, T., Perry, A., Smith, P.T., Jiang, J., and Xiao, T.S. (2013). Structure of the absent in melanoma 2 (AIM2) pyrin domain provides insights into the mechanisms of AIM2 autoinhibition and inflammasome assembly. *J. Biol. Chem.* *288*, 13225–13235.
- Lamkanfi, M., and Dixit, V.M. (2012). Inflammasomes and their roles in health and disease. *Annu. Rev. Cell Dev. Biol.* *28*, 137–161.
- Li, X., Mooney, P., Zheng, S., Booth, C.R., Braunfeld, M.B., Gubbens, S., Agard, D.A., and Cheng, Y. (2013). Electron counting and beam-induced motion correction enable near-atomic-resolution single-particle cryo-EM. *Nat. Methods* *10*, 584–590.
- Lin, S.C., Lo, Y.C., and Wu, H. (2010). Helical assembly in the MyD88-IRAK4-IRAK2 complex in TLR/IL-1R signalling. *Nature* *465*, 885–890.
- Liao, M., Cao, E., Julius, D., and Cheng, Y. (2013). Structure of the TRPV1 ion channel determined by electron cryo-microscopy. *Nature* *504*, 107–112.
- Liepinsh, E., Barbals, R., Dahl, E., Sharipo, A., Staub, E., and Otting, G. (2003). The death-domain fold of the ASC PYRIN domain, presenting a basis for PYRIN/PYRIN recognition. *J. Mol. Biol.* *332*, 1155–1163.
- Masumoto, J., Taniguchi, S., Ayukawa, K., Sarvotham, H., Kishino, T., Niikawa, N., Hidaka, E., Katsuyama, T., Higuchi, T., and Sagara, J. (1999). ASC, a novel 22-kDa protein, aggregates during apoptosis of human promyelocytic leukemia HL-60 cells. *J. Biol. Chem.* *274*, 33835–33838.
- Masumoto, J., Taniguchi, S., and Sagara, J. (2001). Pyrin N-terminal homology domain- and caspase recruitment domain-dependent oligomerization of ASC. *Biochem. Biophys. Res. Commun.* *280*, 652–655.
- Medzhitov, R., and Janeway, C., Jr. (2000). Innate immune recognition: mechanisms and pathways. *Immunol. Rev.* *173*, 89–97.
- Moriya, M., Taniguchi, S., Wu, P., Liepinsh, E., Otting, G., and Sagara, J. (2005). Role of charged and hydrophobic residues in the oligomerization of the PYRIN domain of ASC. *Biochemistry* *44*, 575–583.
- Morrone, S.R., Wang, T., Constantoulakis, L.M., Hooy, R.M., Delannoy, M.J., and Sohn, J. (2013). Cooperative assembly of IFI16 filaments on dsDNA provides insights into host defense strategy. *Proc. Natl. Acad. Sci. USA* *111*, E62–E71.
- Park, H.H., Logette, E., Rauser, S., Cuenin, S., Walz, T., Tschopp, J., and Wu, H. (2007). Death domain assembly mechanism revealed by crystal structure of the oligomeric PIDDosome core complex. *Cell* *128*, 533–546.
- Potter, C.S., Chu, H., Frey, B., Green, C., Kisseberth, N., Madden, T.J., Miller, K.L., Nahrstedt, K., Pulokas, J., Reilein, A., et al. (1999). Legimon: a system for fully automated acquisition of 1000 electron micrographs a day. *Ultramicroscopy* *77*, 153–161.
- Qiao, Q., Yang, C., Zheng, C., Fontán, L., David, L., Yu, X., Bracken, C., Rosen, M., Melnick, A., Egelman, E.H., and Wu, H. (2013). Structural architecture of the CARMA1/Bcl10/MALT1 signalosome: nucleation-induced filamentous assembly. *Mol. Cell* *51*, 766–779.
- Rathinam, V.A., Vanaja, S.K., and Fitzgerald, K.A. (2012). Regulation of inflammasome signaling. *Nat. Immunol.* *13*, 333–342.
- Rosenthal, P.B., and Henderson, R. (2003). Optimal determination of particle orientation, absolute hand, and contrast loss in single-particle electron cryomicroscopy. *J. Mol. Biol.* *333*, 721–745.
- Saitoh, T., Fujita, N., Jang, M.H., Uematsu, S., Yang, B.G., Satoh, T., Omori, H., Noda, T., Yamamoto, N., Komatsu, M., et al. (2008). Loss of the autophagy protein Atg16L1 enhances endotoxin-induced IL-1 $\beta$  production. *Nature* *456*, 264–268.
- Schröder, G.F., Brunger, A.T., and Levitt, M. (2007). Combining efficient conformational sampling with a deformable elastic network model facilitates structure refinement at low resolution. *Structure* *15*, 1630–1641.
- Stehlik, C., Krajewska, M., Welsh, K., Krajewski, S., Godzik, A., and Reed, J.C. (2003). The PAAD/PYRIN-only protein POP1/ASC2 is a modulator of ASC-mediated nuclear-factor-kappa B and pro-caspase-1 regulation. *Biochem. J.* *373*, 101–113.
- Strowig, T., Henao-Mejia, J., Elinav, E., and Flavell, R. (2012). Inflammasomes in health and disease. *Nature* *481*, 278–286.
- Theile, C.S., Witte, M.D., Blom, A.E., Kundrat, L., Ploegh, H.L., and Guimaraes, C.P. (2013). Site-specific N-terminal labeling of proteins using sortase-mediated reactions. *Nat. Protoc.* *8*, 1800–1807.
- Touitou, I., Lesage, S., McDermott, M., Cuisset, L., Hoffman, H., Dode, C., Shoham, N., Aganna, E., Hugot, J.P., Wise, C., et al. (2004). Infervers: an evolving mutation database for auto-inflammatory syndromes. *Hum. Mutat.* *24*, 194–198.
- Wu, H. (2013). Higher-order assemblies in a new paradigm of signal transduction. *Cell* *153*, 287–292.
- Yin, Q., Sester, D.P., Tian, Y., Hsiao, Y.S., Lu, A., Cridland, J.A., Sagulenko, V., Thygesen, S.J., Choubey, D., Hornung, V., et al. (2013). Molecular mechanism for p202-mediated specific inhibition of AIM2 inflammasome activation. *Cell Rep.* *4*, 327–339.
- Yuan, S., and Akey, C.W. (2013). Apoptosome structure, assembly, and pro-caspase activation. *Structure* *21*, 501–515.
- Zhou, Z.H. (2011). Atomic resolution cryo electron microscopy of macromolecular complexes. *Adv. Protein Chem. Struct. Biol.* *82*, 1–35.

## **SUPPLEMENTAL INFORMATION**

# **Unified Polymerization Mechanism for the Assembly of ASC-dependent Inflammasomes**

Alvin Lu, Venkat Giri Magupalli, Jianbin Ruan, Qian Yin, Maninjay K. Atianand, Matthijn Vos, Gunnar F. Schröder, Katherine A. Fitzgerald, Hao Wu\* and Edward H. Egelman

\* Correspondence to hao.wu@childrens.harvard.edu

## **Inventory of Supplemental Information**

### **SUPPLEMENTAL FIGURES**

Figure S1. Related to Figure 1;  
Figure S2. Related to Figure 2;  
Figure S3. Related to Figure 3;  
Figure S4. Related to Figure 4;  
Figure S5. Related to Figure 5;  
Figure S6. Related to Figure 6;  
Figure S7. Related to Figure 7.

### **SUPPLEMENTAL TABLES**

Table S1, related to Figure 4;  
Table S2, related to Figure 5;  
Table S3, related to Figure 5;  
Table S4, related to Figure 7.

### **SUPPLEMENTAL MOVIE**

Movie S1, related to Figure 3.

### **SUPPLEMENTAL EXPERIMENTAL PROCEDURES**

### **SUPPLEMENTAL REFERENCES**

**SUPPLEMENTAL FIGURES**

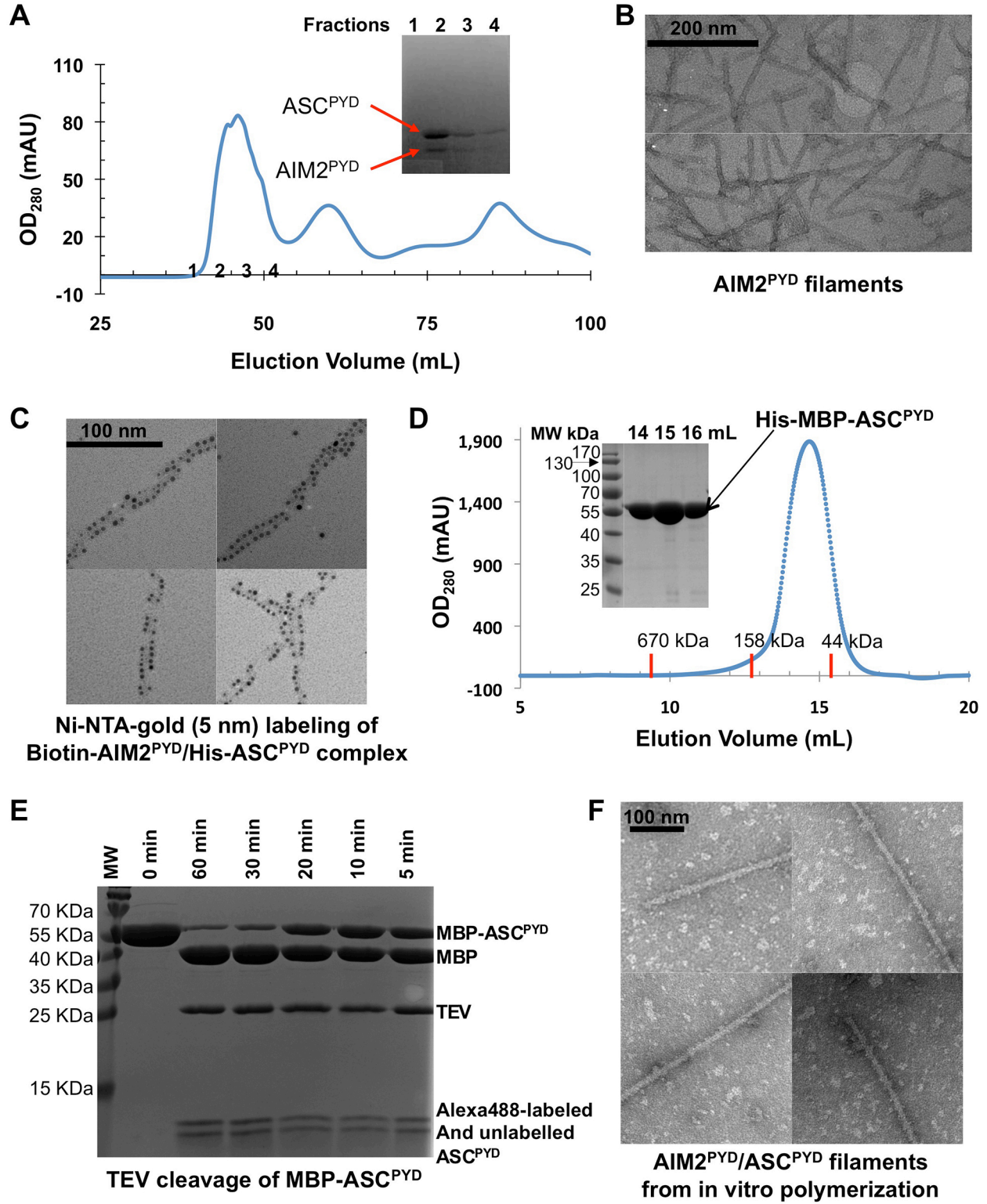


**Figure S1. ASC<sup>PYD</sup> Forms filamentous Structures as Visualized by Electron Microscopy, Related to Figure 1**

- A.** Size-exclusion chromatograph of the ASC<sup>PYD</sup>/AIM2<sup>PYD</sup> complex. ASC<sup>PYD</sup> is fused with an N-terminal His-tag and co-expressed with untagged AIM2<sup>PYD</sup>. The complex was first purified by Ni-affinity chromatography. It elutes in the void position on a Superdex 200 gel filtration column.
- B.** A negative stain EM image of Sumo-AIM2<sup>PYD</sup> filaments.
- C.** Ni-NTA-gold (5 nm) labeling of Biotin-AIM2<sup>PYD</sup>/His-ASC<sup>PYD</sup> complex.
- D.** Size-exclusion chromatography of His-MBP tagged ASC<sup>PYD</sup>. His-MBP-ASC<sup>PYD</sup> fusion protein is monomeric on a Superdex200 column.
- E.** Proteolysis time course of MBP-tagged ASC<sup>PYD</sup> labeled with Alexa488 by the TEV protease.
- F.** AIM2<sup>PYD</sup> nucleated ASC<sup>PYD</sup> filaments after the *in vitro* polymerization assay.

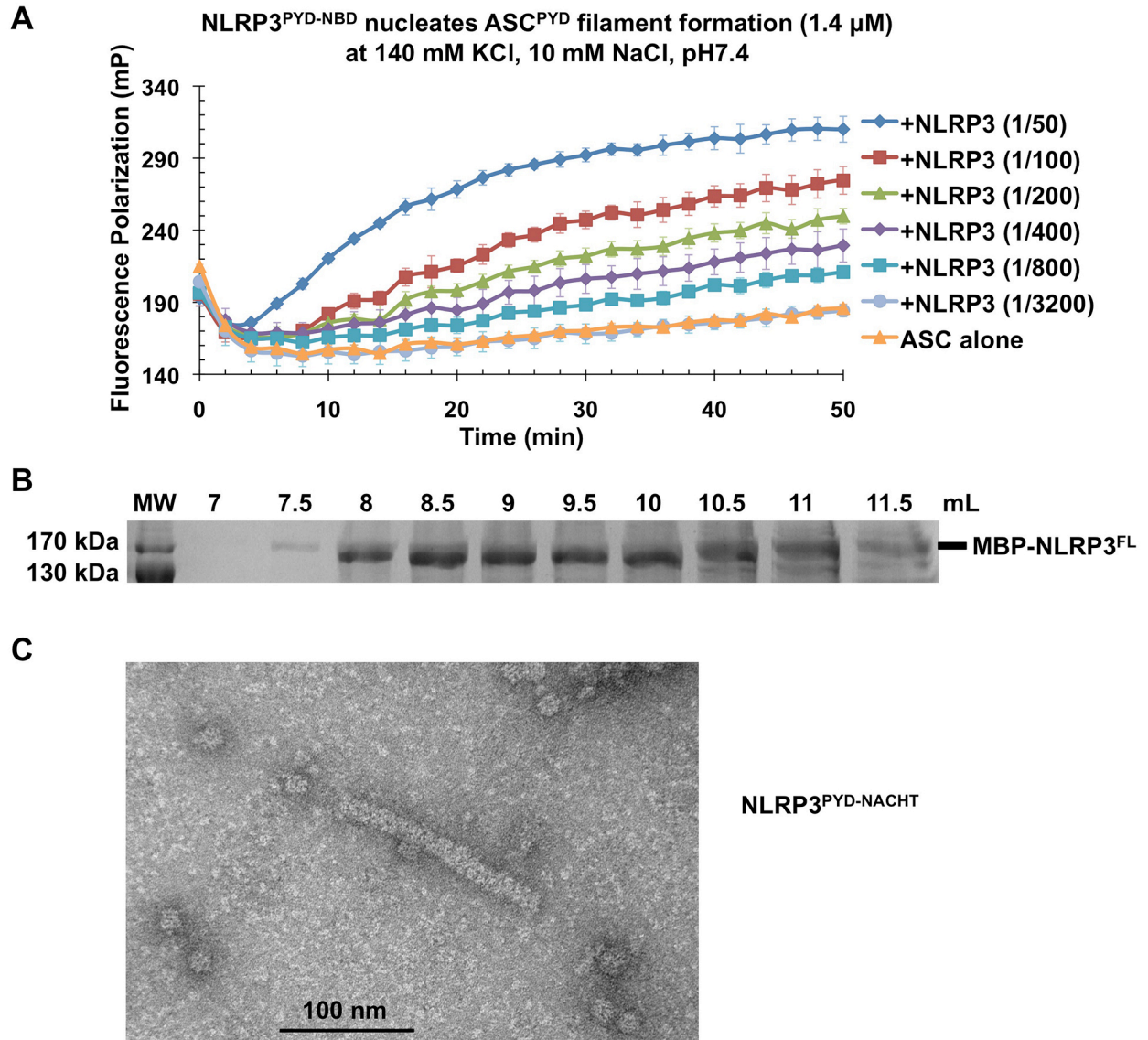


**Figure S2. NLRP3<sup>FL</sup> and NLRP3<sup>PYD-NBD</sup> but not NLRP3<sup>PYD</sup> Promote ASC<sup>PYD</sup> Filament Formation, Related to Figure 2**

**A.** NLRP3<sup>PYD-NBD</sup> nucleates ASC<sup>PYD</sup> filament formation (1.4  $\mu$ M) at the physiological intracellular condition of 140 mM KCl and 10 mM NaCl at pH7.4. Data are represented as mean $\pm$ SD (N=3).

**B.** SDS-PAGE of size-exclusion chromatography fractions of insect cell expressed MBP-NLRP3<sup>FL</sup>.

**C.** A negative stain EM image of recombinant NLRP3<sup>PYD-NBD</sup>.

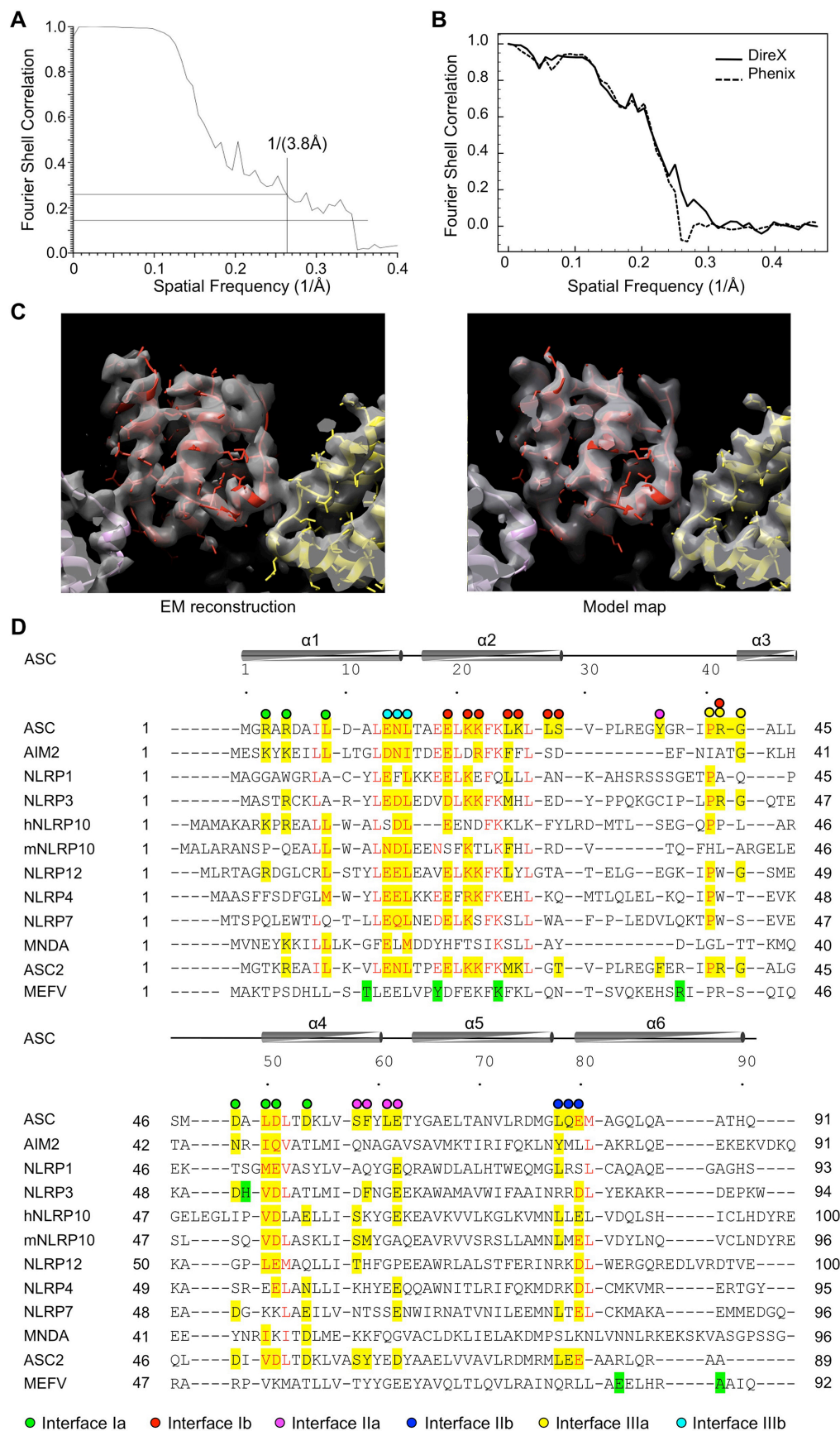


**Figure S3. Cryo-EM Structure of the ASC<sup>PYD</sup> Filament at Near Atomic Resolution, Related to Figure 3**

**A.** Fourier shell correlation (FSC) plot of the reconstruction, generated by dividing the images into two halves.

**B.** FSC plot of ASC<sup>PYD</sup> filament reconstruction generated by comparison of the cryo-EM map with the final model, using DireX with occupancy refinement (solid line) and Phenix with TLS refinement (dashed line). The former gave a nominal resolution of 3.6 Å at FSC=0.143.

**C.** The actual EM reconstruction, filtered to 3.8 Å, is shown on the left as a transparent grey surface. Three adjacent subunits are shown as a ribbon model, each in a different color. On the right, the grey surface is that generated from the model when filtered to 3.8 Å and with refinement by DireX. The comparison shows that the 3.8 Å resolution, as claimed, is reasonable.

**D.** Structure-based sequence alignment of 11 PYDs with known structures. These include PYDs of ASC (Liepinsh et al., 2003), NLRP1 (Hiller et al., 2003), ASC2 (Espejo and Patarroyo, 2006; Natarajan et al., 2006), hNLRP10 (Su et al., 2013), mNLRP10 (PDB code 2DO9), NLRP7 (Pinheiro et al., 2010), NLRP12 (Pinheiro et al., 2011), NLRP3 (Bae and Park, 2011), NLRP4 (Eibl et al., 2012), MNDA (PDB code: 2DBG) and AIM2 (Jin et al., 2013). Residues conserved in more than 7 proteins are shown in red. Yellow-highlighted residues indicate conservation with those in the ASC<sup>PYD</sup> interfaces. The PYD of MEFV (also known as Pyrin), whose mutations are associated with FMF, is included at the bottom of the alignment. Locations of disease mutations in NLRP3 and pyrin are highlighted in green.

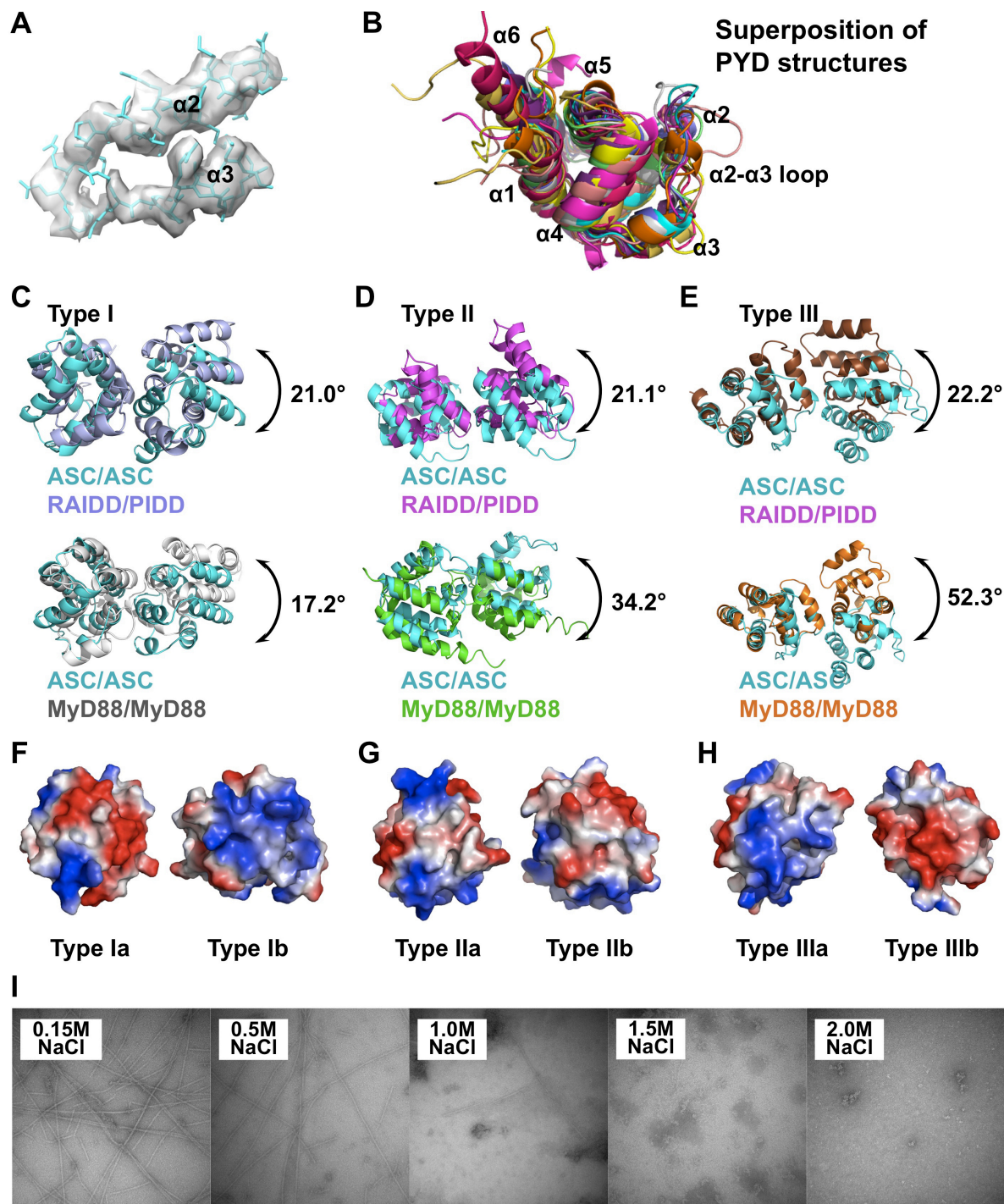


**Figure S4. Detailed Cryo-EM Model of the ASC<sup>PYD</sup> Filament, Related to Figure 4**

**A.** Cryo-EM density superimposed with ASC<sup>PYD</sup> structure in the filament in the α2-α3 region

**B.** Superposition of all 11 known PYD structures, showing the short α3 and the variation at the α2-α3 loop.

**C, D, E.** Superposition of the ASC/ASC dimers with RAIDD/PIDD dimers (top) and MyD88/MyD88 dimers (bottom) in the type I (**C**), type II (**D**) and type III (**E**) interactions.

**F, G, H.** Electrostatic surface representation of the interaction patches.

**I.** High salt significantly disrupts filament formation.

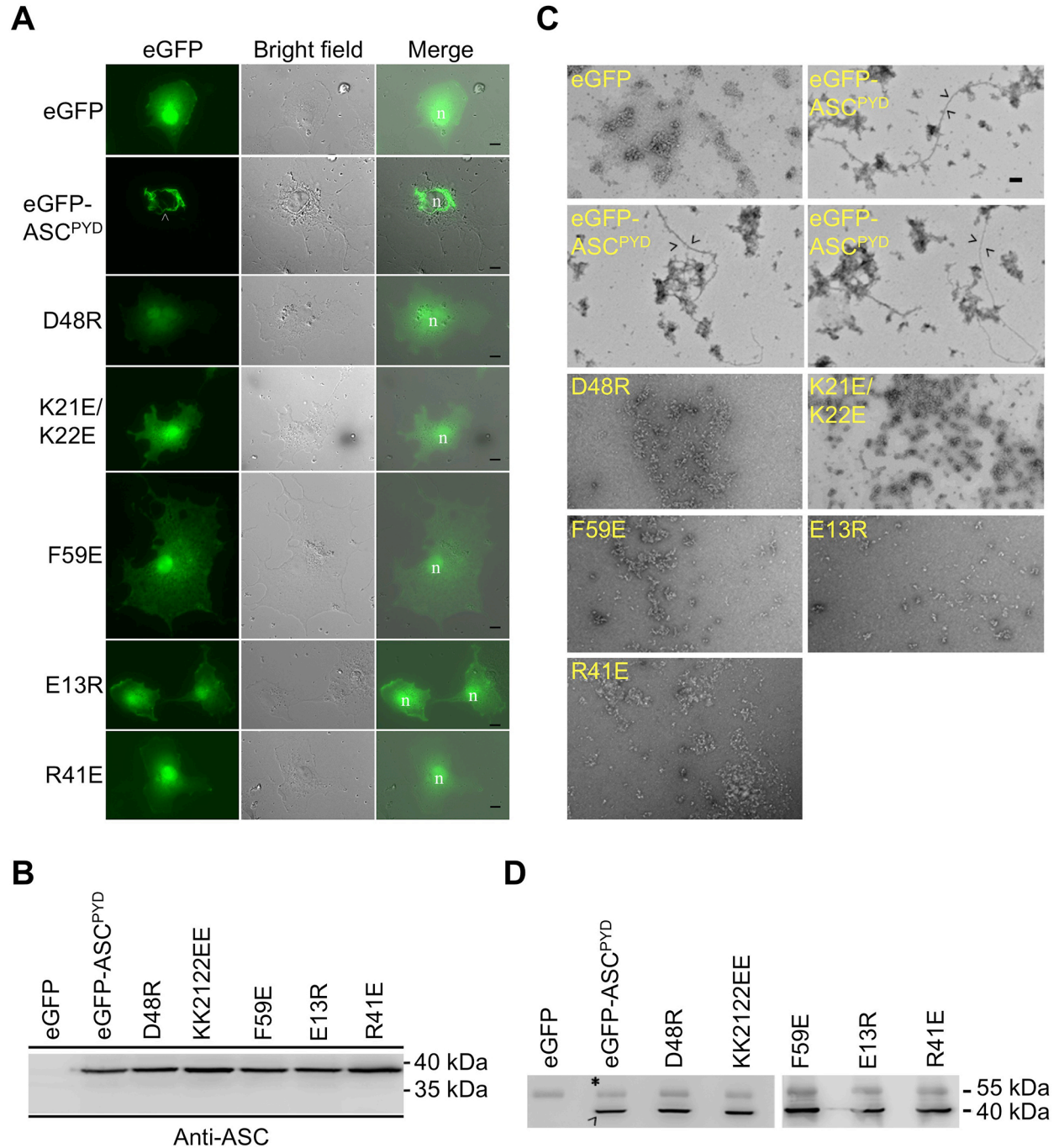


**Figure S5. Structure-based Mutations Disrupts ASC Filament Formation and AIM2/ASC and NLRP3/ASC Interactions *in Vitro* and in Cells, Related to Figure 5**

**A.** Morphology of ASC<sup>PYD</sup> filaments visualized by fluorescence microscopy. eGFP control, WT (the arrowhead depicts filaments) and mutant (D48R, K21E/K22E, F59E, E13R and R41E) eGFP-tagged ASC<sup>PYD</sup> (1-106) constructs were expressed in COS-1 cells. n: nucleus; scale bars = 10  $\mu$ m.

**B.** Expression levels of depicted constructs shown by Western blotting using anti-ASC specific antibody.

**C.** Morphology of ASC<sup>PYD</sup> filaments visualized by EM. eGFP control, WT and mutant (D48R, K21E/K22E, F59E, E13R and R41E) eGFP-tagged ASC<sup>PYD</sup> constructs were expressed in HEK 293T cells. ASC immunoprecipitated complex was eluted followed by negative stain EM visualization. Scale bar = 100 nm.

**D.** ASC immunoprecipitated complex was eluted and analyzed by Western blotting using anti-ASC specific antibody. Lower band at ~40 kDa (denoted by arrowhead) represents eluted ASC, and upper band at ~55 kDa represents IgG heavy chain (denoted by asterisk).

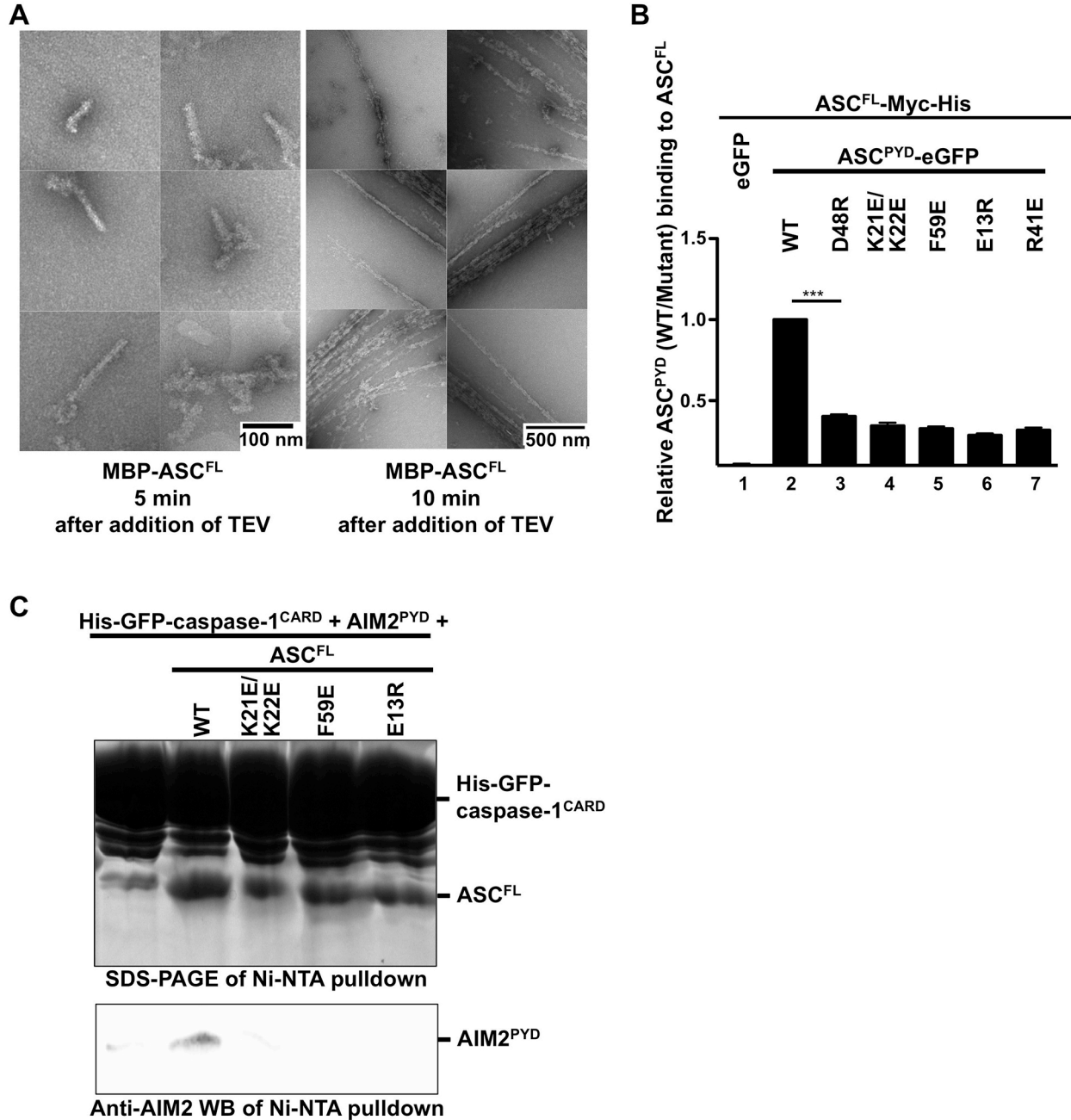


**Figure S6. Reconstitution of Full AIM2 Inflammasome, Related to Figure 6**

**A.** Kinetics of ASC<sup>FL</sup> aggregation upon removal of the His-MBP tag.

**B.** Quantification of relative ASC<sup>PYD</sup> (Mutant/WT) binding to ASC<sup>FL</sup> using anti-eGFP antibody, shown as mean ± S.E. \*\*\* denotes  $p < 0.001$  by Student's  $t$  test,  $n=4$ .

**C.** Ni-NTA pulldown of AIM2<sup>PYD</sup> by His-GFP-caspase-1<sup>CARD</sup> through WT or mutant ASC<sup>FL</sup> with mutations in the PYD. GFP-caspase-1<sup>CARD</sup>, MBP-ASC<sup>FL</sup>, and MBP-AIM2<sup>PYD</sup> were incubated on ice overnight with TEV protease. MBP and uncut MBP-AIM2<sup>PYD</sup> and MBP-ASC<sup>FL</sup> were removed by incubating with amylose resin for 1 hr. Unbound fractions were incubated with Ni-NTA resin for 1 hr, washed 3 times, eluted and subjected to SDS-PAGE.

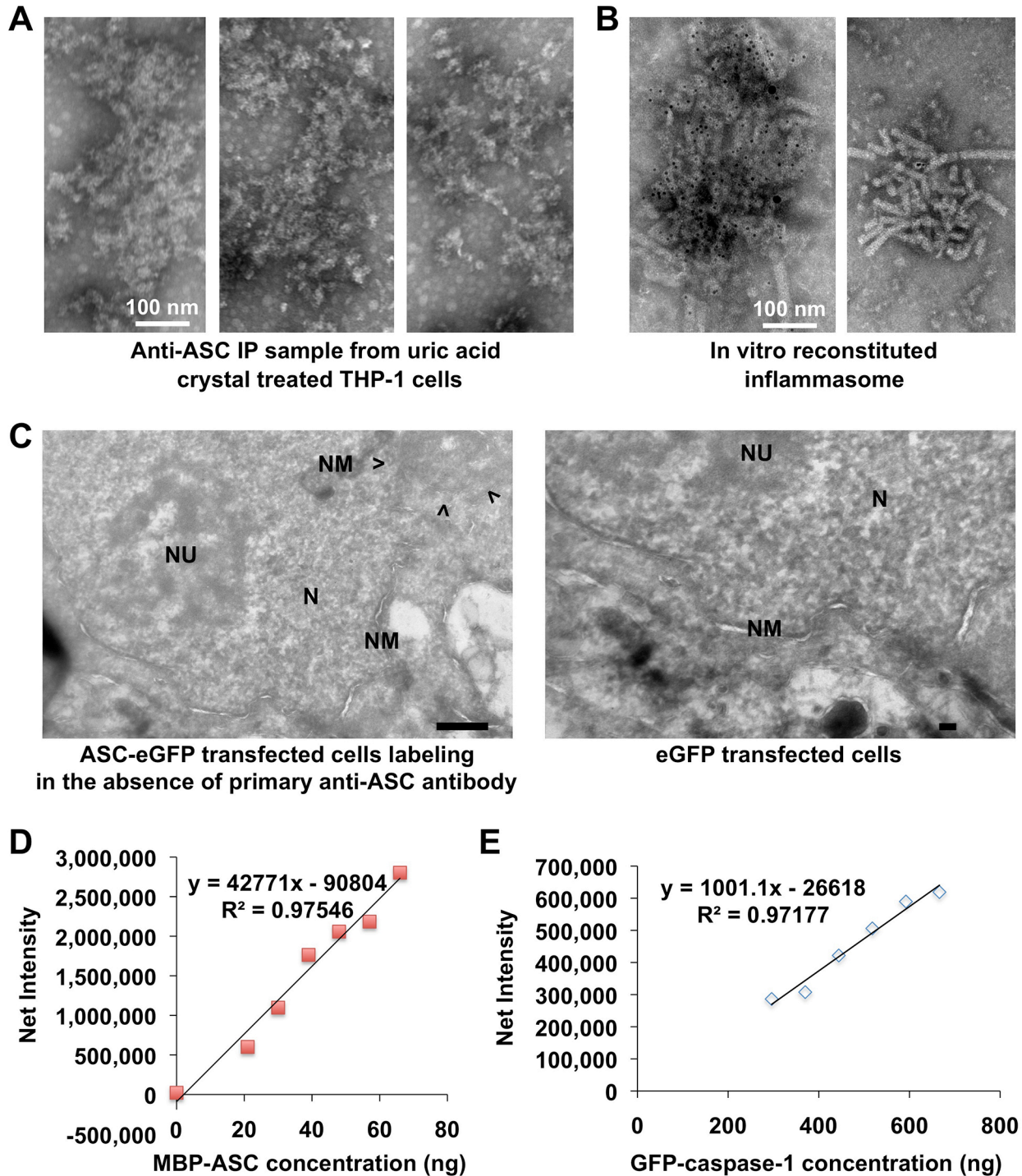


**Figure S7. Morphology, Stoichiometry and ProIL-1 $\beta$  Processing in Inflammasomes, Related to Figure 7**

**A, B.** Morphology of anti-ASC immunoprecipitated NLRP3 inflammasome clusters from uric acid crystal activated THP-1 cells analyzed by negative stain EM (A) in comparison with in vitro reconstituted inflammasomes incubated overnight (B).

**C.** Control images of immunogold EM on ultrathin cryosections. Left: Lack of labeling in the ASC-eGFP transfected cells in the absence of primary anti-ASC antibody. Arrowheads

delineate perinuclear punctum. Right: eGFP alone transfected cells showed neither punctum nor anti-ASC gold labeling. Scale bar: 500 nm

**D.** Standard curve of quantitative Western blot of recombinant His-MBP-ASC.

**E.** Standard curve of quantitative Western blot of recombinant His-GFP-caspase-1.

## SUPPLEMENTAL TABLES

**Table S1. Comparison Between Interactions in the ASC<sup>PYD</sup> Filament and Those in the PIDDosome and the Myddosome, Related to Figure 4.** Shown are rotations needed to match the second subunit when the first subunit in the interaction pairs is aligned, Summary: 15-21° for type I, 21-35° for type II and 17-52° for type III interactions.

	ASC/ASC_Type I	ASC/ASC_Type II	ASC/ASC_Type III
PIDDosome			
RAIDD/RAIDD	16.2°	22.5°	33.2°
RAIDD/PIDD	21.0°	21.1°	22.2°
PIDD/PIDD	15.1°	N/A	17.9°
Myddosome			
MyD88/MyD888	17.2°	34.2°	52.3°
MyD88/IRAK4	25.5°	35.3°	35.4°
IRAK4/IRAK2	20.3°	22.4°	41.6°

**Table S2. Summary of Mutagenesis Results on ASC<sup>PYD</sup> Interfaces, Related to Figure 5. -:** disruption of filament formation; +/-: weakening of filament formation.

	Residues	Structure-based mutants <i>in vitro</i>	Structure-based mutants in cells	Existing defective mutants (Moriya et al., 2005)
<b>Type I</b>				
Ia	R3	R3E (+/-)		
Ia	R5			
Ia	L9			
Ia	D48	D48R (-), D48N (-)	D48R (-)	D48A, D48N, D48E, D48R
Ia	L50	L50A (+/-)		
Ia	D51	D51R (-)		D51A, D51N, D51K
Ia	D54			
Ib	E19			E19A
Ib	K21	K21Q (-)		K21A, K21Q, K21E
Ib	K22	K21E/K22E (-)	K21E/K22E (-)	
Ib	L25			
Ib	K26	K26E (-)		K26A, K26Q
Ib	L28			
Ib	S29			
Ib	R41	R41E (-)	R41E (-)	R41A, R41Q, R41W
<b>Type II</b>				
IIa	Y36	Y36A (+/-)		
IIa	S58			
IIa	F59	F59E (-)	F59E (-)	
IIa	L61			
IIa	E62			E62A
IIb	L78			
IIb	Q79			
IIb	E80	E80R (+/-)		
<b>Type III</b>				
IIIa	P40			
IIIa	R41	R41E (-)	R41E (-)	R41A, R41Q, R41W
IIIa	G42			
IIIb	E13	E13R (-)	E13R (-)	
IIIb	N14			
IIIb	L15			

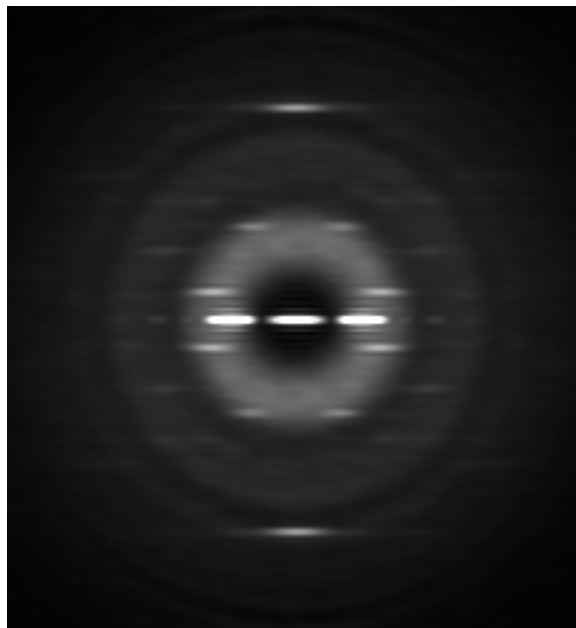
**Table S3. Relative Rates of ASC<sup>PYD</sup> Polymerization in the Presence of Sub-stoichiometric NLRP3 or AIM2, Related to Figure 5.** Control rate: rate of ASC<sup>PYD</sup> filament formation in the absence of nucleator. Nucleation rate: initial rate of filament formation in the presence of nucleator. +: indicates normal nucleation; +/-: indicates partially defective nucleation; -: indicates abolishment of nucleation

Activator	Mutation	Interface	Nucleation Ability	Polymerization rate ratio between with and without the activator
NLRP3 <sup>PYD-NBD</sup>	WT (@1/100 molar ratio)		+	10.61
	K23E,K24E	Type Ib	-	1.10
	M27E	Type Ib	-	0.88
	E64R	Type IIa	-	0.98
	D82R	Type IIb	-	1.02
	R43W	Type IIIa	-	1.11
	E15R	Type IIIb	-	0.98
AIM2 <sup>PYD</sup>	WT (@1/4 molar ratio)		+	4.91
	L10A,L11A	Type Ia	-	0.87
	R24E	Type Ib	-	0.95
	F27G	Type Ib	-	1.54
	Y74R	Type IIb	-	1.17
	G38E	Type IIIa	+/-	2.39
	K39E	Type IIIa	+/-	2.92
	D15R	Type IIIb	-	1.12

**Table S4. Structure-based Sequence Alignment of PYDs Relative to ASC<sup>PYD</sup> Shows Conservation and Variability at the Three Asymmetric Interfaces, Related to Figure 7.** The number of residues conserved with ASC<sup>PYD</sup> and the total number of residues at each interface are shown in the table and in parentheses, respectively. The total percentages of conservation are shown in the right column for those PYDs with  $\geq 50\%$  homology to ASC. See Figure S3C for the alignment.

	Ia (7)	Ib (7)	IIa (5)	IIb (3)	IIIa (3)	IIIb (3)	Total (28)
AIM2	6	3	0	1	1	3	14, 50%
NLRP1	2	3	1	1	1	2	10
NLRP3	4	4	2	1	3	3	17, 61%
hNLRP10	6	1	2	2	1	2	14, 50%
mNLRP10	3	2	2	2	0	3	12
NLRP12	4	4	1	1	2	3	15, 54%
NLRP4	3	3	1	1	1	3	12
NLRP7	2	2	1	2	1	3	11
MNDA	4	0	0	0	0	2	6
ASC2	6	6	4	3	3	3	25, 89%

## SUPPLEMENTAL MOVIE



### Movie S1. Averaged Power Spectrum Animation, Related to Figure 3

This three-frame animation was generated by computing the averaged power spectrum from filament segments in the central three bins of the histogram in Figure 3C. The large shifts of the near-equatorial layer line ( $n=-6$ ) as well as the almost fixed meridional intensity (at  $\sim 1/14 \text{ \AA}^{-1}$ ) arise from a variable twist with little variability in the axial rise per subunit. The power spectra, which are unbiased (due to the fact that they are invariant under translations of the images and do not require alignments of the images), demonstrate that the sorting in Figure 3C worked properly.

## SUPPLEMENTAL EXPERIMENTAL PROCEDURES

## Recombinant Protein Expression and Purification

Various methods were attempted to obtain high quality filaments of ASC<sup>PYD</sup>. The best results were obtained with ASC<sup>PYD</sup> (residues 1-106), which was cloned into pDB-His-MBP vector (Berkeley Structural Genomics Center) using the NdeI and NotI cloning sites and expressed as an MBP-fusion protein with an additional N-terminal 6 x His tag. This construct was transformed and expressed in BL21(DE3) cells by growing the culture at 37 °C to OD of 0.8 and inducing with 0.5 mM IPTG overnight at 16 °C. The *E. coli* cells were harvested and lysed by sonication in a buffer containing 20 mM Tris at pH 8.0, 200 mM NaCl, 5 mM imidazole, 5 mM β-ME, and 10% glycerol. The cell lysate was centrifuged at 40,000 g for 40 minutes. The supernatant containing soluble MBP-ASC<sup>PYD</sup> fusion protein was passed through a pre-equilibrated Ni-NTA column by gravity. The column was washed with 20 column-volume sonication buffer containing 20 mM imidazole. The fusion protein was eluted from the Ni-NTA beads with sonication buffer containing 300mM imidazole and passed through a Superdex 200 10/300 GL size-exclusion column with elution buffer containing 20 mM HEPES, 150 mM NaCl, and 1 mM TCEP. To avoid aggregation, all the purification steps were carried out at 4 °C.

The ASC<sup>PYD</sup> filaments were formed by cleavage of the MBP tag with TEV protease at a molar ratio of 1/10 of the fusion protein. This reaction was left overnight at room temperature, which resulted in complete cutting and no precipitation. Cleaved MBP and TEV were removed by passing this mixture through a small Ni-NTA column. The flow-through, containing ASC<sup>PYD</sup> filaments formed *in vitro*, was diluted accordingly for EM studies.

For nucleation assay, NLRP3<sup>PYD-NBD</sup> construct (residues 2-550) was over-expressed in BL21(DE3) cells with an N-terminal His-MBP tag and purified by Ni-NTA resin followed by gel filtration. The void peak (about 7-8 ml fractions) was concentrated for assay. All mutations in this construct were introduced using the QuikChange mutagenesis protocol. NLRP3<sup>FL</sup> was cloned into a modified pFastBac HTa vector containing an N-terminal His-MBP tag. This construct was expressed in High Five cells (Invitrogen) with the Bac-to-Bac system using a manufacturer-recommended protocol. Lysis and purification steps were the same as above. AIM2<sup>FL</sup> and AIM2<sup>PYD</sup> (residues 1-100) were cloned into pDB-His-MBP vector and over-expressed in BL21(DE3) cells with an N-terminal MBP tag. Mutants for FP assay were generated by QuikChange mutagenesis. AIM2<sup>FL</sup> were purified by Ni-NTA resin followed by gel filtration. Only fractions corresponding to the monomeric position were used for assay. MBP-tagged AIM2<sup>PYD</sup> wildtype and mutant constructs were expressed as monomer for assay and pulldown purposes (see below).

## ASC<sup>PYD</sup> Polymerization Assay

Since ASC<sup>PYD</sup> contains no cysteine residue for convenient labeling, a cysteine residue was introduced to C-terminus of the above MBP-ASC<sup>PYD</sup> fusion construct (S106C) by QuikChange mutagenesis. This fusion protein was expressed and purified similarly to the wildtype except a buffer at pH 7.0 was used during the gel filtration step. About 30 nmol of the purified protein was incubated with a Cys-reactive fluorophore, Alexa Fluor 488 C<sub>5</sub> maleimide, with 2-fold excess. The reaction was left overnight on ice and passed through a Superdex 200 to remove excess dye. The fraction containing labeled fusion protein was diluted to about 2 to 3 μM for assay in a black round-bottom 384-well Greiner Bio-One plate.

For each well, three parts of labeled fusion protein was added to one part of reaction buffer containing 20 mM HEPES pH 8.0, 150 mM NaCl, 1 mM TCEP, 1 % Triton-X100, and other reaction components (such as TEV, nucleator proteins, DNA, and/or ATP). Data were collected with the SpectraMax M5e Multi-Mode Microplate Reader (Molecular Devices) using excitation at 495 nm and emission at 519 nm with an auto-cutoff filter at 515 nm.

## Caspase-1<sup>CARD</sup> Polymerization Assay

Labeling caspase-1<sup>CARD</sup> by Alexa Fluor 488 C<sub>5</sub> maleimide abolished filament formation due to three exposed cysteine residues on the surface of the molecule. We used the sortase method (Theile et al., 2013) for labeling the monomeric “sandwich”-tagged caspase-1<sup>CARD</sup> (N-terminal MBP, C-terminal Sumo). Labeling reagents, including an engineered, Ca<sup>2+</sup>-independent sortase and the peptide-fluorophore conjugate Gly-Gly-Gly-TAMRA (GGG-TAMRA), were kindly provided by Dr. Hidde Ploegh. MBP-caspase-1<sup>CARD</sup>-Sumo containing a C-terminal sortase motif, “LPETGG”, was purified to homogeneity similar to the ASC<sup>PYD</sup> construct. Two mg of the gel filtration monomer was incubated in a mixture containing protein: sortase: GGG-TAMRA = 50 μM: 30 μM: 500 μM at 4°C overnight. The labeled MBP-casp1<sup>CARD</sup>-Sumo was separate from free peptide-fluorophore by gel filtration in 20 mM HEPES pH 8.0, 150 mM NaCl, and 1 mM TCEP. MBP-tagged ASC<sup>PYD</sup>, ASC<sup>CARD</sup>, and ASC<sup>FL</sup> in this assay were purified as monomer in the same buffer by gel filtration. Upon removal of the MBP tag, caspase-1<sup>CARD</sup> polymerized into filaments and the C-terminal Sumo did not interfere with filament formation (as confirmed by EM). TAMRA labeled caspase-1 was used at ~4 μM in this assay. The same setup as the ASC<sup>PYD</sup> polymerization assay was used with excitation/emission at 561 nm/585 nm.

### Binary PYD/PYD Complexes and Nanogold Labeling

To form the AIM2<sup>PYD</sup>/ASC<sup>PYD</sup> binary complex, the two gene fragments (AIM2 1-100, ASC 1-106) were inserted into the pDW363 biotinylation vector (Tsao et al., 1996) to co-express AIM2<sup>PYD</sup> with an N-terminal biotin acceptor peptide (BAP) and ASC<sup>PYD</sup> with an N-terminal 6 x His tag. The vector contains the BirA enzyme gene for AIM2<sup>PYD</sup> biotinylation *in vivo*. The complex was expressed in BL21(DE3) cells. Similar expression protocol as above was used except that during overnight induction, 50 μM of biotin was supplemented. Since ASC<sup>PYD</sup> forms filaments inside the *E. coli* cells resulting in reduced solubility compared to monomeric proteins, a lower speed (30,000 g for 30min) was used for clarifying the cell debris after sonication. The complex was purified by Ni-NTA resin with the batch method followed by gel filtration.

For the NLRP3<sup>PYD-NACT</sup>/ASC<sup>PYD</sup> complex, a different approach was used. NLRP3<sup>PYD-NBD</sup> (residues 2-550) was cloned into a modified pDB-His-MBP vector containing the biotin acceptor peptide. This construct was expressed with an N-terminal His-MBP tag and a C-terminal BAP and biotinylated *in vivo* by co-expressing with the empty pDW363 vector (harboring the BirA enzyme) using the co-transformation method. The biotinylated NLRP3<sup>PYD-NBD</sup> was mixed with 50-fold excess of the monomeric MBP-fused ASC<sup>PYD</sup>. The polymerization of ASC<sup>PYD</sup> was achieved by adding TEV to cleave off the MBP tag, forming the NLRP3<sup>PYD-NBD</sup>/ASC<sup>PYD</sup> complex.

Nanogold labeling for biotinylated binary complexes was done using streptavidin-gold conjugate (Electron Microscopy Sciences, 6 nm diameter gold). A carbon-coated copper EM grid was covered with 5 μl of sample and let sit for 1 minute. Excess sample was blotted with filter paper, and the grid was washed upside-down on 25 μl of incubation buffer (20 mM HEPES pH 8.0, 150 mM NaCl, 1 mM TCEP, and 0.1 % gelatin) three times of 1 minute each. The grid was floated for 60 minutes on 25 μl of 6 nm streptavidin-gold conjugate diluted in incubation buffer for 60 minutes. The grid was washed three times with incubation buffer and stained for 1 minute in 2 % uranyl acetate. Images were taken on a Tecnai G<sup>2</sup> Spirit BioTWIN Electron Microscope.

### Ternary Complexes and Immunogold Labeling

MBP-fused ASC<sup>FL</sup>, MBP-fused AIM2<sup>PYD</sup>, and GFP-fused caspase-1<sup>CARD</sup> were expressed separately in BL21(DE3) cells and purified by Ni-NTA resin and gel filtration chromatography. The ternary complex was formed *in vitro* by mixing AIM2/ASC/caspase-1 in a ratio of 1:1:3 and incubating with TEV for 2 hrs in room temperature to cleave off the MBP tag. The mixture was passed through amylose resin to remove cleaved MBP tag and uncut ASC<sup>FL</sup> and AIM2<sup>PYD</sup>. The complex was purified by Ni-NTA resin using 6 x His-GFP as a handle. Untagged ASC<sup>FL</sup> and AIM2<sup>PYD</sup> in the core ternary complex were detected by Western blot.

Visualization of AIM2 and ASC were achieved by immunogold labeling using appropriate commercially available primary antibodies (rabbit polyclonal IgG, against PYD). After applying 5  $\mu$ L of samples, the grids were washed with incubation buffer (gel filtration buffer + 0.1 % gelatin) for three times of 1 minute each. The grids were floated on respective primary antibody diluted to appropriate concentrations recommended by EMS for immunogold labeling (for anti-AIM2, 0.5  $\mu$ g/ml; for anti-ASC, 2  $\mu$ g/ml). After 1 hr incubation, grids were washed three times with incubation buffer, then floated on 25  $\mu$ L of secondary antibody-gold conjugate (goat anti-rabbit IgG, either 15 nm or 6 nm) diluted 1/20 in incubation buffer for 1 hr. The grids were washed and stained for 1 minute in uranyl acetate for visualization. For caspase-1 labeling, Ni-NTA-nanogold conjugate (Nanoprobes, 5nm) was incubated with the ternary complex on grid for 30 minutes (similar to the streptavidin-gold labeling).

### **Cryo-Electron Microscopy and Image Processing**

Samples (2.5  $\mu$ l) were applied to glow-discharged lacey carbon grids and vitrified using an FEI Vitrobot Mark IV. Grids were imaged using an FEI Titan Krios electron microscope operating at 300 keV, and recorded using a 4k x 4k Falcon II direct electron detector with a backthinned CMOS chip, with a sampling of 1.08  $\text{\AA}/\text{px}$ . The CTFFIND3 program (Mindell and Grigorieff, 2003) was used for determining the defocus, which ranged from  $\sim 1.0 \mu$  to  $\sim 4.0 \mu$ . A total of 370 images were used. The e2helixboxer routine from EMAN2 (Tang et al., 2007) was used for boxing filaments from the images. These long filaments were then cut into overlapping boxes, each 400 px (432  $\text{\AA}$ ) long, with a shift of 20 px between adjacent boxes (an overlap of 380 px). The SPIDER software package (Frank et al., 1996) was used for most of the image processing, and the IHRSR algorithm (Egelman, 2000) was implemented within SPIDER. The helical indexing was unambiguous (Egelman, 2010) due to the strong meridional intensity at  $\sim 1/(13.9 \text{\AA})$  in averaged power spectra, showing that the rise per asymmetric unit in the filament was  $\sim 13.9 \text{\AA}$ . The layer line at  $\sim 1/(31 \text{\AA})$  is  $n=3$ , and the near-equatorial layer line is  $n=-6$ . There is a C3 point-group symmetry, so every layer line contains a Bessel order that is a multiple of three. An initial reconstruction was generated using this symmetry. The broadness of the  $n=-6$  layer line in the averaged power spectrum, combined with the sharpness of the meridional layer line, suggested that the filaments had a fairly constant axial rise but a variable twist (Egelman and DeRosier, 1982). We therefore generated multiple references, having different values of the twist and axial rise, to use for a reference-based sorting of the images. The results showed that almost all of the variation was in the twist, as suspected, and power spectra generated from bins with different twists confirm the sorting (movie S1). Using references with a spacing of  $0.3^\circ$  in twist, the central bin (with a twist of  $52.9^\circ$ ) had 24,665 segments among the  $\sim 80,000$  total segments, and these were used for the final reconstruction.

Without treating out-of-plane tilt, the reconstruction reached a resolution of  $\sim 6-7 \text{\AA}$ . The absolute hand of the reconstruction was unambiguous at this resolution given the comparison with the NMR structure (1UCP.PDB). Using references with out-of-plane tilt showed that the mode of the distribution was  $\sim 6^\circ$  of tilt from the normal to the beam. The final cycles of the IHRSR algorithm involved generating references with azimuthal angle and out-of-plane tilt increments of  $1.5^\circ$ . The symmetry converged to a twist of  $52.91^\circ$  and an axial rise of  $13.95 \text{\AA}$ . The stated resolution of  $\sim 3.8 \text{\AA}$  has been determined by comparison with the atomic model which provides a reality-check on any claims, absent from the Fourier Shell Correlation (FSC) approach (Yu et al., 2012). It is clear, however, that the resolution is not uniform, and the helices on the inside of the filament that are more tightly packed are better resolved than those on the outside. The right-handed nature of the  $\alpha$ -helices is clearly visible. The standard FSC method (dividing the data into two sets, aligned against the same reference) yielded  $\text{FSC} = 0.26$  at  $1/(3.8 \text{\AA})$ , while the resolution at  $\text{FSC} = 0.143$  (Rosenthal and Henderson, 2003) gave a resolution of  $2.9 \text{\AA}$ .

## Structural Refinement

The ASC<sup>PYD</sup> NMR structure (PDB ID 1UCP) (Liepinsh et al., 2003) was chosen as the starting model for refinement. A region of the filament EM density with a length of 108 Å was extracted and 15 protomers were docked as a rigid-body into the EM density. The radial structure factor distribution of the EM density was then scaled to match that of the 15 subunit starting model. The density was then further sharpened with a B-factor of  $-60 \text{ \AA}^2$  and a cosine shaped smooth cutoff at a resolution of 3.5 Å was applied.

The model was optimized by iterations over real-space refinement in DireX (Schröder et al., 2007) and manual model building with Coot (Emsley and Cowtan, 2004). For the refinement, a mask was generated by computing a 15 Å density map from the initial atomic model. The edges of this low resolution density were steepened by applying a cosine mapping function with the program apply-cos-mapping, which is part of DireX, using the values 0.4 and 0.3 as upper and lower threshold values, respectively. A simple Babinet bulk solvent model with  $k_{sol} = 0.65$  and  $B_{sol} = 45 \text{ \AA}^2$  was used.

A cross-validation approach was used to identify the optimally fitted model and to prevent over fitting (Falkner and Schröder, 2013). In brief, only Fourier components of the cryo-EM density map lower than 3.7 Å were used for fitting, while Fourier components from the so called 'free' interval 3.5–3.7 Å were used for validation only. For this, the cross-correlation coefficient,  $C_{free}$ , is calculated between the model density map and the cryo-EM density map, both of which were band-pass filtered using the free interval, thus containing information that has not been used for fitting.

To further assist model building and correction a 20 ns MD simulation was performed using Gromacs (Hess et al., 2008) with the Amber99SB-ILDN force field (Lindorff-Larsen et al., 2010). The simulation included 12 protomers solvated in explicit water. From this simulation, 1200 snapshots of structures were extracted and refined with DireX into the EM density. The structure with the lowest  $C_{free}$  value was compared with the refined NMR model and the fragment between residues 31 to 53 fitted significantly better into the density was therefore used to replace the corresponding fragment in the model.

For final refinement, 20 iterations over DireX refinement and energy minimization with CNS (Brunger, 2007) (without experimental data) were performed. The DireX refinement used grouped and restrained occupancy refinement. This final refinement procedure yields  $C_{work}$  and  $C_{free}$  values of 0.826 and 0.108, respectively. The Fourier Shell Correlation (FSC) between the final model and the EM density yields a cross-resolution of 3.6 Å, 4.8 Å, and 5.9 Å for FSC=0.143, 0.5, and 0.71 criteria. Phased reciprocal space refinement with Phenix (Adams et al., 2010) including TLS refinement resulted in a very similar FSC curve (Figure S3A). Resolution measurements have been much more problematic and controversial in the EM field than in X-ray crystallography, and attempts have been made to devise measures when there is no atomic model that can be compared to the reconstruction (Sousa and Grigorieff, 2007). However, when near atomic resolution is achieved, we think that the ultimate measure of resolution is provided by the interpretability of the map and the comparison between the model and the map (Figure S3B, S3C). Therefore, based upon both the FSC (Figure S3A) and the comparisons of the map with the model (Figure S3B, S3C), we estimate the resolution of our reconstruction at  $\sim 3.8 \text{ \AA}$ .

## Plasmids and Antibodies

Full length human ASC was cloned in EcoRI/XhoI sites of pCDNA3.1/myc-HisA and XhoI/HindIII sites of pEGFP-N1. ASC PYD (residues 1-106) (WT), encoding the PYD domain of human ASC, was amplified via PCR using full-length human ASC as template. The PCR product was cloned into the XhoI/HindIII sites of pEGFP-N1. Mutants (D48R, KK2122EE, F59E, E13R, R41E, K21E/D48K/D51K and E67R) of ASC<sup>PYD</sup> (1-106) domain were generated by standard sit-

directed mutagenesis kit (Stratagene). These mutants were cloned into the XhoI/HindIII sites of pEGFP-N1. All constructs were sequence verified.

The following antibodies were diluted and used as described below: anti-EGFP, 1:5,000 (polyclonal, Thermo Scientific); anti-ASC (N-15), 1:5,000 (polyclonal, Santa Cruz Biotechnology); anti-caspase-1 p12 subunit, 1:5,000 (monoclonal, Thermo Scientific).

### **Cell Culture and Transfection**

The cells were grown in 100 mm dish and six-well plate containing coverslip for protein extraction and morphological studies respectively. HEK 293T cells were grown in DMEM with L-glutamine supplemented with 10 % fetal bovine serum. COS-1 cells were grown in DMEM supplemented with 10 % fetal bovine serum. THP-1 cells were maintained in RPMI with L-glutamine supplemented with 10 % fetal bovine serum, and 0.1 mM non-essential amino acids solution. All cells were maintained at 37 °C with 5 % CO<sub>2</sub>. COS-1 and HEK 293T cells were transfected using Lipofectamine 2000 (Invitrogen) according to the manufacture's instructions.

For NLRP3 inflammasome activation, THP-1 cells were treated overnight with PMA (300 ng/ml final concentration). This was followed by overnight LPS induction (10 µg/ml final concentration). Uric acid crystals (200 µg/ml final concentration) treatment was carried out for 6 hours. During whole procedure cells were maintained at 37 °C with 5 % CO<sub>2</sub>.

### **Protein Extraction, Immunoprecipitation, Immunoblotting, and Electron Microscopy**

Wildtype and mutant (D48R, KK2122EE, F59E, E13R and R41E) human ASC<sup>PYD</sup> domain (residue 1-106) constructs were expressed in HEK 293T cells, and were processed for recombinant protein extraction as follows. The Petri dishes were placed on ice, and cells were harvested with a rubber scraper and sedimented at ~2,600 g at 4 °C for 20 min. Cells were washed once with 20 ml of ice-cold PBS to remove serum proteins. The cell pellet was resuspended in 500 µl of lysis buffer (50 mM Tris-HCl, pH 7.5, 150 mM NaCl, 5 mM EGTA, 5 mM EDTA, and protease inhibitor) and pipetted up and down 10 times. The preparation was sedimented at ~500 g at 4 °C for 5 min to remove the nuclear fraction. The supernatant was collected and resedimented at 16,000 g at 4 °C for 30 min. The supernatant was measured for protein concentration with Bradford assay, and normalized to 1 mg/ml.

For immunoprecipitation, the precleared supernatant was immunoprecipitated with anti-ASC antibody overnight at 4 °C. The immobilized immune complex on protein A-sepharose was washed thrice using 1 ml of lysis buffer, and eluted using 0.2 M glycine at pH 2.6. Samples were immediately neutralized with Tris-HCl at pH 8.0. The eluted immunopurified complex was resuspended in 5 µl of 5 x sample buffer and heated at 95 °C for 5 min. Proteins were resolved on 12.5 % SDS-PAGE gels, and immunoblotting was performed with anti-ASC and anti-eGFP antibodies.

Co-immunoprecipitation experiments were performed in transfected HEK 293T cells. Precleared supernatants were immunoprecipitated with monoclonal anti-His antibodies (Qiagen), overnight at 4 °C. The immobilized immune complex on protein A-sepharose was washed thrice using 1 ml of lysis buffer. The bound complex was eluted using 20 µl of 5 x sample buffer and heated at 95 °C for 5 min. Proteins were resolved on 12.5 % SDS-PAGE gels, and immunoblotting was performed with anti-His antibodies, and co-immunoprecipitated component was detected using polyclonal anti-eGFP antibodies (Thermo Scientific). Western blots (ECL detection) were documented using Chemidoc MP system (BioRad). Binding was quantified using densitometric measurement of band intensity using NIH ImageJ software.

For negative staining electron microscopy, glow discharged copper grids containing 2 µl of eluted immunopurified complex were stained with 5 % uranyl acetate for 1 minute and air-dried. Samples were imaged using JEOL 1200EX 80kV Transmission Electron Microscope (TEM) and images were recorded with an AMT 2k CCD camera (Harvard Medical School core facility).

### **Fluorescence and Confocal Laser Scanning Microscopy**

COS-1 cells were seeded at a density of  $2 \times 10^5$  for morphological studies. 12 hours post transfection cells were monitored by Zeiss Axiovert 135 fluorescence microscope (Carl Zeiss) at various time points. Cells were washed once with PBS, fixed with 4 % PFA for 5 minutes at room temperature, and were mounted in *N*-propyl gallate (NPG) antifade. Fluorescence microscopy was performed using a Zeiss Axiovert 200M microscope (Carl Zeiss) equipped for conventional epifluorescence microscopy with the respective filter sets for enhanced green fluorescent protein (eGFP). Images were captured using a 40 x objective (0.75 numerical aperture) with AxioVision Rel. 4.6 software. Confocal sections were obtained with confocal laser scanning microscope FluoView FV1000 (Olympus). Images were captured using a 60 x objective (1.2 numerical aperture) with Olympus FluoView version 3.0 viewer software. The images were identically processed with Adobe Photoshop.

### **Immunogold EM on Ultrathin Cryosections**

Transfected COS-1 cells (human ASC full length-eGFP and eGFP alone) were used for immunogold electron microscopy as previously described (Griffiths, 1993) and as detailed below. For preparation of cryosections the cells were rinsed once with PBS and were removed from the dish using 0.5mM EDTA (PBS). 800  $\mu$ l of the cell suspension was layered on top of a 200  $\mu$ l cushion of 8 % paraformaldehyde (in 0.1 M Sodium Phosphate buffer, pH 7.4) in an eppendorf tube and was sedimented at  $\sim$ 510 g for 3 minutes at room temperature (RT). The supernatant was carefully removed and fresh 4 % paraformaldehyde was added. Cells were fixed for 2 hours at room temperature and later fixative was replaced with PBS. Prior to freezing in liquid nitrogen the cell pellets were infiltrated with 2.3 M sucrose (PBS) (containing 0.2 M glycine to quench free aldehyde groups) for 15 minutes at RT. Frozen samples were sectioned at  $-120$  °C, the sections were transferred to formvar-carbon coated copper grids. Grids were floated on 2 % gelatin dish at 4 °C until the immunogold labeling was carried out. The gold labeling was carried out at RT on a piece of parafilm. Grids were floated on drops of 1 % BSA for 10 minutes to block for unspecific labeling, transferred to 5  $\mu$ l drops of primary antibody (anti-ASC, 1:50) and was incubated for overnight at 4 °C. The grids were then washed in 4 drops of PBS for a total of 15 minutes, transferred to 5  $\mu$ l drops of Protein-A gold (10 nm) for 20 minutes, washed in 4 drops of PBS for 15 minutes and 6 drops of double distilled water at RT. Protein-A gold (10 nm) labeling alone served as a control. The labeled sections were contrasted by floating the grids on drops of 0.3% uranyl acetate in 2% methyl cellulose for 10 minutes, the excess liquid was removed with a filterpaper (Whatman #1), leaving a thin coat of methyl cellulose (bluish interference color when dry). The grids were examined in a JEOL 1200EX-80kV Transmission electron microscope (TEM) and images were recorded with an AMT 2k CCD camera (Harvard Medical School core facility).

### **AIM2 Inflammasome Reconstitution**

Transient reconstitution of the human AIM2 inflammasome was performed as previously described (Burckstummer et al., 2009; Hornung et al., 2009; Jin et al., 2012). In brief, HEK293T cells were transfected with pEFBOS-C-term-Guassia luciferase/Flag pro-IL-1 $\beta$  (~54 kDa), pro-caspase-1, HA-ASC, and the full-length wildtype or mutant Flag-AIM2 expression constructs using GeneJuice (Novagen). Cell lysates were probed with mouse anti-IL1 $\beta$  monoclonal antibody (clone 3zD, National Cancer Institute, NIH). Expression of ASC and AIM2 was detected using anti-Flag (Sigma) and anti-HA antibodies (Roche Applied Biosystems), respectively.

## **SUPPLEMENTAL REFERENCES**

Adams, P.D., Afonine, P.V., Bunkoczi, G., Chen, V.B., Davis, I.W., Echols, N., Headd, J.J., Hung, L.W., Kapral, G.J., Grosse-Kunstleve, R.W., *et al.* (2010). PHENIX: a comprehensive Python-based system for macromolecular structure solution. *Acta Crystallogr D Biol Crystallogr* **66**, 213-221.

Bae, J.Y., and Park, H.H. (2011). Crystal structure of NALP3 protein pyrin domain (PYD) and its implications in inflammasome assembly. *J Biol Chem* **286**, 39528-39536.

Brunger, A.T. (2007). Version 1.2 of the Crystallography and NMR system. *Nat Protoc* **2**, 2728-2733.

Burckstummer, T., Baumann, C., Bluml, S., Dixit, E., Durnberger, G., Jahn, H., Planyavsky, M., Bilban, M., Colinge, J., Bennett, K.L., *et al.* (2009). An orthogonal proteomic-genomic screen identifies AIM2 as a cytoplasmic DNA sensor for the inflammasome. *Nat Immunol* **10**, 266-272.

Egelman, E.H. (2000). A robust algorithm for the reconstruction of helical filaments using single-particle methods. *Ultramicroscopy* **85**, 225-234.

Egelman, E.H. (2010). Reconstruction of helical filaments and tubes. *Methods Enzymol* **482**, 167-183.

Egelman, E.H., and DeRosier, D.J. (1982). The Fourier transform of actin and other helical systems with cumulative random angular disorder. *Acta Cryst A* **38**, 796-799.

Eibl, C., Grigoriu, S., Hessenberger, M., Wenger, J., Puehringer, S., Pinheiro, A.S., Wagner, R.N., Proell, M., Reed, J.C., Page, R., *et al.* (2012). Structural and Functional Analysis of the NLRP4 Pyrin Domain. *Biochemistry* **51**, 7330-7341.

Emsley, P., and Cowtan, K. (2004). Coot: model-building tools for molecular graphics. *Acta Crystallogr D Biol Crystallogr* **60**, 2126-2132.

Espejo, F., and Patarroyo, M.E. (2006). Determining the 3D structure of human ASC2 protein involved in apoptosis and inflammation. *Biochem Biophys Res Commun* **340**, 860-864.

Falkner, B., and Schröder, G.F. (2013). Cross-validation in cryo-EM-based structural modeling. *Proc Natl Acad Sci U S A* *in press*.

Frank, J., Radermacher, M., Penczek, P., Zhu, J., Li, Y., Ladjadj, M., and Leith, A. (1996). SPIDER and WEB: processing and visualization of images in 3D electron microscopy and related fields. *J Struct Biol* **116**, 190-199.

Griffiths, G. (1993). *Fine Structure Immunocytochemistry* (Heidelberg, Germany, Springer Verlag).

Hess, B., Kutzner, C., van der Spoel, D., and Lindahl, E. (2008). GROMACS 4: Algorithms for Highly Efficient, Load-Balanced, and Scalable Molecular Simulation. *J Chem Theory Comput* **4**, 435-447.

Hiller, S., Kohl, A., Fiorito, F., Herrmann, T., Wider, G., Tschopp, J., Grutter, M.G., and Wuthrich, K. (2003). NMR structure of the apoptosis- and inflammation-related NALP1 pyrin domain. *Structure (Camb)* **11**, 1199-1205.

Hornung, V., Ablasser, A., Charrel-Dennis, M., Bauernfeind, F., Horvath, G., Caffrey, D.R., Latz, E., and Fitzgerald, K.A. (2009). AIM2 recognizes cytosolic dsDNA and forms a caspase-1-activating inflammasome with ASC. *Nature* **458**, 514-518.

Jin, T., Perry, A., Jiang, J., Smith, P., Curry, J.A., Unterholzner, L., Jiang, Z., Horvath, G., Rathinam, V.A., Johnstone, R.W., *et al.* (2012). Structures of the HIN domain:DNA complexes reveal ligand binding and activation mechanisms of the AIM2 inflammasome and IFI16 receptor. *Immunity* **36**, 561-571.

Jin, T., Perry, A., Smith, P.T., Jiang, J., and Xiao, T.S. (2013). Structure of the AIM2 pyrin domain provides insights into the mechanisms of AIM2 autoinhibition and inflammasome assembly. *J Biol Chem*.

Liepinsh, E., Barbals, R., Dahl, E., Sharipo, A., Staub, E., and Otting, G. (2003). The death-domain fold of the ASC PYRIN domain, presenting a basis for PYRIN/PYRIN recognition. *J Mol Biol* **332**, 1155-1163.

Lindorff-Larsen, K., Piana, S., Palmo, K., Maragakis, P., Klepeis, J.L., Dror, R.O., and Shaw, D.E. (2010). Improved side-chain torsion potentials for the Amber ff99SB protein force field. *Proteins* 78, 1950-1958.

Mindell, J.A., and Grigorieff, N. (2003). Accurate determination of local defocus and specimen tilt in electron microscopy. *J Struct Biol* 142, 334-347.

Moriya, M., Taniguchi, S., Wu, P., Liepinsh, E., Otting, G., and Sagara, J. (2005). Role of charged and hydrophobic residues in the oligomerization of the PYRIN domain of ASC. *Biochemistry* 44, 575-583.

Natarajan, A., Ghose, R., and Hill, J.M. (2006). Structure and dynamics of ASC2, a pyrin domain-only protein that regulates inflammatory signaling. *J Biol Chem* 281, 31863-31875.

Pinheiro, A.S., Eibl, C., Ekman-Vural, Z., Schwarzenbacher, R., and Peti, W. (2011). The NLRP12 pyrin domain: structure, dynamics, and functional insights. *J Mol Biol* 413, 790-803.

Pinheiro, A.S., Proell, M., Eibl, C., Page, R., Schwarzenbacher, R., and Peti, W. (2010). Three-dimensional structure of the NLRP7 pyrin domain: insight into pyrin-pyrin-mediated effector domain signaling in innate immunity. *J Biol Chem* 285, 27402-27410.

Rosenthal, P.B., and Henderson, R. (2003). Optimal determination of particle orientation, absolute hand, and contrast loss in single-particle electron cryomicroscopy. *J Mol Biol* 333, 721-745.

Schröder, G.F., Brunger, A.T., and Levitt, M. (2007). Combining efficient conformational sampling with a deformable elastic network model facilitates structure refinement at low resolution. *Structure* 15, 1630-1641.

Sousa, D., and Grigorieff, N. (2007). Ab initio resolution measurement for single particle structures. *J Struct Biol* 157, 201-210.

Su, M.Y., Chang, C.I., and Chang, C.F. (2013). (1)H, (13)C and (15)N resonance assignments of the pyrin domain from human PYNOD. *Biomol NMR Assign*.

Tang, G., Peng, L., Baldwin, P.R., Mann, D.S., Jiang, W., Rees, I., and Ludtke, S.J. (2007). EMAN2: an extensible image processing suite for electron microscopy. *J Struct Biol* 157, 38-46.

Theile, C.S., Witte, M.D., Blom, A.E., Kundrat, L., Ploegh, H.L., and Guimaraes, C.P. (2013). Site-specific N-terminal labeling of proteins using sortase-mediated reactions. *Nat Protoc* 8, 1800-1807.

Tsao, K.L., DeBarbieri, B., Michel, H., and Waugh, D.S. (1996). A versatile plasmid expression vector for the production of biotinylated proteins by site-specific, enzymatic modification in *Escherichia coli*. *Gene* 169, 59-64.

Yu, X., Goforth, C., Meyer, C., Rachel, R., Wirth, R., Schroder, G.F., and Egelman, E.H. (2012). Filaments from *Ignicoccus hospitalis* show diversity of packing in proteins containing N-terminal type IV pilin helices. *J Mol Biol* 422, 274-281.